MANCHESTER 1824
The University of Manchester

Extended Coupled Cluster approach to Twisted Graphene Layers

A dissertation submitted to The University of Manchester for the degree of
Master of Science by Research in Theoretical Physics
in the Faculty of Science and Engineering

Year of submission
2023

Ingvars Vitenburgs

School of Natural Sciences
Department of Physics and Astronomy

Contents

Word count: 11500

Abstract

Correlated systems are usually studied using the normal coupled cluster method. Unfortunately, this method is only a small subset of the actual description of such systems, with symmetry-breaking, required for studying phase transitions, not permitted. Additionally, in the strong correlation regime it is known to breakdown. Therefore, in this dissertation a workflow for the extended coupled cluster framework is presented up to doubles truncation. This is done using the particle-hole formalism in order to produce manageable algebra with automatic differentiation as a way to solve the equations. It is further discussed to be equivalent to adding correlation treatment directly to Hartree-Fock. A novel study of correlation effects in twisted bilayer graphene is presented as a practical application. This is accomplished by using the Bistritzer-MacDonald model with a double metallic gate potential to account for electrostatic interactions in an experimental setting. Simulations at singles truncation agreed with previous Hartree-Fock studies, while correlation effects at doubles truncation showed insignificant contributions to the band structure, but a relatively significant increase of the Fermi level, indicating lower filling requirements for the phase transition. Tensor contraction is suggested as a way to significantly reduce the computational cost of this workflow and permit studies of valley and spin effects as well as other larger systems.

Declaration of originality

I hereby confirm that this dissertation is my own original work unless referenced clearly to the contrary, and that no portion of the work referred to in the dissertation has been submitted in support of an application for another degree or qualification of this or any other university or other institute of learning.

Intellectual property statement

i The author of this thesis (including any appendices and/or schedules to this thesis) owns certain copyright or related rights in it (the "Copyright") and s/he has given The University of Manchester certain rights to use such Copyright, including for administrative purposes.

ii Copies of this thesis, either in full or in extracts and whether in hard or electronic copy, may be made *only* in accordance with the Copyright, Designs and Patents Act 1988 (as amended) and regulations issued under it or, where appropriate, in accordance with licensing agreements which the University has from time to time. This page must form part of any such copies made.

iii The ownership of certain Copyright, patents, designs, trademarks and other intellectual property (the "Intellectual Property") and any reproductions of copyright works in the thesis, for example graphs and tables ("Reproductions"), which may be described in this thesis, may not be owned by the author and may be owned by third parties. Such Intellectual Property and Reproductions cannot and must not be made available for use without the prior written permission of the owner(s) of the relevant Intellectual Property and/or Reproductions.

iv Further information on the conditions under which disclosure, publication and commercialisation of this thesis, the Copyright and any Intellectual Property and/or Reproductions described in it may take place is available in the University IP Policy (see `http://documents.manchester.ac.uk/DocuInfo.aspx?DocID=24420`), in any relevant Dissertation restriction declarations deposited in the University Library, and The University Library's regulations (see `http://www.library.manchester.ac.uk/about/regulations/_files/Library-regulations.pdf`).

1 Introduction

Quantum many-body techniques are used to analytically, and possibly numerically, describe various nanoscale systems with the main objective, in comparison with experimental science, of understanding the underlying processes at a level that cannot be directly measured, subsequently calculating properties that can.

The earliest such method [1] can be dated back to 1928 - the Hartree-Fock method. Since then many others have been developed, with different balances between accuracy and speed. Some notable examples are density functional theory [2] described by Hohenberg and Kohn in 1964, several post Hartree-Fock methods, such as coupled cluster, redefined by Čížek [3] for electronic structure calculations in 1966, several versions of quantum Monte Carlo methods, with their origins even tracing back [4] to the 1950s and etc. An interesting modern-day development by Carleo and Troyer [5] includes using reinforcement-learning techniques for this problem.

In this dissertation, expressions and simulation procedures are developed for the extended coupled cluster method [6]–[11]. This is done using the particle-hole formalism, in order to produce manageable algebra. The goal is therefore to add consideration of correlation effects directly to the Hartree-Fock method, which is only partly present in normal coupled cluster. This is especially important for strongly correlated systems with phase transitions, in order to allow symmetry-breaking. While it is possible to implement coupled cluster on top of Hartree-Fock [12], this only provides a quantitative analysis. Another small area of development, presented here, is the use of automatic differentiation [13], [14] in minimizing energy functionals in quantum many-body techniques. This has the potential to decrease the amount of work required for developing these kinds of new methods.

To show the newly developed method in action, a suitable candidate - twisted bilayer graphene - is computationally described with the use of a low energy continuum model [15], [16]. The causes of superconducting and insulating phases, recently discovered [17], [18] in this system, are of great interest. Recent Hartree-Fock studies [19], [20] suggest that long range electrostatic interactions play a significant role in this system and thus correlation effects need to be accounted for as well. While there is a even more recent coupled cluster study [21] looking at this, methods that permit symmetry-breaking should be used, because of the aforementioned phase transitions. It is worth noting the most recent work on this problem, exploring the introduction of magnetic orderings into the continuum approximation [22] and conservation of instantaneous two-point correlation functions in the random phase approximation method [23].

Additionally, studies of correlation effects of trapped electrons in one dimension and single layer graphene are presented here as well, mainly for educational purposes of the author. It may be argued that the use of the Ewald summation technique, in calculating electrostatic effects for graphene, might be excessive and is present for educational purposes as well.

2 Example Application of Quantum Many-Body Methods

The one dimensional electron gas is a fundamental problem and an ideal candidate to study quantum many-body techniques. Therefore, in this section the performance of Hartree-Fock and the coupled cluster method is compared for this problem, with exact diagonalisation used as a reference in the case of 3 particles. Further, the more complex case of 15 particles is presented. Both, ground and excited, state properties are examined.

2.1 Interacting Electrons in a Infinite 1D Well

It is well known [24] that the static properties of quantum systems are determined by the stationary Schrödinger equation

$$\hat{H}|\Psi\rangle = E|\Psi\rangle \tag{1}$$

In the case of a single electron, trapped in an infinite well of width L, it can be easily shown that the resulting wavefunction is

$$\langle\psi_n|x\rangle = \begin{cases} \sqrt{\frac{2}{L}}\sin\left(\frac{n\pi}{L}x\right) & \text{if } x \in [0, L] \\ 0 & \text{otherwise} \end{cases} \tag{2}$$

While this solution set is obviously valid for only a single electron, it can serve as a good set of basis functions. This means that a solution in the case of N electrons for a state with quantisation numbers $\{m_i\}$ and coordinates $\{x_i\}$ can be expressed as a linear superposition of these functions

$$\langle\psi_{\{m_i\}}|x_1, x_2, \ldots, x_N\rangle = \sum_{\{n_i\}} C^{\{n_i\}}_{\{m_i\}} \prod_{i=1}^{N} \langle\psi_{n_i}|x_i\rangle \tag{3}$$

Here summation is done over all possible sets of quantisation numbers $\{n_i\}$. For an exact solution, all n_i would go up to infinity, so in practice truncation is applied, only taking into account states up to a certain level: $n_i \in [1, n_{\text{max}}]$. The methods, described further in this subsection, are essentially different ways of calculating coefficients $C_{\{n_i\}}$, whilst balancing between accuracy and performance.

The N electron Hamiltonian for the system described above is given by

$$\hat{H} = -\sum_{i=1}^{N} \frac{\hbar^2}{2m_e}\partial_i^2 - \sum_{i\neq j}^{N} \frac{e^2}{4\pi\epsilon_0|x_i - x_j|} \tag{4}$$

To ease calculations, this can be rewritten in second quantisation [25], using the single particle basis described above

$$\hat{H} = \sum_{n=1}^{n_{max}} n^2 \hat{a}_n^\dagger \hat{a}_n + \frac{1}{4}\sum_{pqrs}^{n_{max}} \langle pq||rs\rangle \hat{a}_p^\dagger \hat{a}_q^\dagger \hat{a}_s \hat{a}_r \tag{5}$$

For computational convenience, energy and length scales in this expression and further have been re-defined in terms of the ground state energy of a single trapped electron $\frac{h^2}{8mL^2}$ and Bohr radius a_0. Here $\langle pq||rs\rangle$ are the anti-symmetrized (due to the fermionic nature of the problem) potential matrix elements

$$\langle pq||rs\rangle = \frac{8L}{\pi^3}\int_0^\pi \int_0^\pi \frac{\sin(px)\sin(qy)[\sin(rx)\sin(sy) - \sin(sx)\sin(ry)]}{|x-y|}dxdy \tag{6}$$

This rank 4 tensor can be easily evaluated numerically using the *quad* function, part of the SciPy [26] software library. Additionally, it is easy to spot that only elements with $|p-q| = |r-s|$ are non-zero and $\langle pq||rs\rangle = -\langle qp||rs\rangle = -\langle pq||sr\rangle = \langle qp||sr\rangle$.

2.2 Quantum Many-Body Methods

2.2.1 Exact Diagonalization

Exact diagonalization is one of the most precise methods in many-body quantum physics. Unfortunately, as will be seen further, it is only practically applicable to small problems. The idea is to expand the interacting wavefunction $\langle\psi_{nml}|x_1, x_2, x_3\rangle$ in terms of all unique permutations of an appropriate multi-particle basis functions $\langle\psi|x\rangle$. For example, a non-interacting one, defined by the Slater determinant. In the case of three particles, which will be used as a reference to compare to Hartree-Fock and coupled cluster, this can be written as

$$\begin{aligned}\langle\psi_{nml}|x_1,x_2,x_3\rangle = \sum_{a<b<c}^{n_{max}} \frac{C_{nml}^{abc}}{\sqrt{6}}(&\langle\psi_a|x_1\rangle\langle\psi_b|x_2\rangle\langle\psi_c|x_3\rangle - \langle\psi_a|x_1\rangle\langle\psi_b|x_3\rangle\langle\psi_c|x_2\rangle + \\ &+\langle\psi_a|x_2\rangle\langle\psi_b|x_3\rangle\langle\psi_c|x_1\rangle - \langle\psi_a|x_2\rangle\langle\psi_b|x_1\rangle\langle\psi_c|x_3\rangle + \langle\psi_a|x_3\rangle\langle\psi_b|x_1\rangle\langle\psi_c|x_2\rangle - \\ &-\langle\psi_a|x_3\rangle\langle\psi_b|x_2\rangle\langle\psi_c|x_1\rangle)\end{aligned} \tag{7}$$

The solution is found by first obtaining the Hamiltonian matrix elements in terms of this basis

$$
\begin{aligned}
(\hat{H}_{ED})_{abc,a'b'c'} = \langle abc|\hat{H}|a'b'c'\rangle = \langle 0|\hat{a}_a\hat{a}_b\hat{a}_c\hat{H}\hat{a}^\dagger_{c'}\hat{a}^\dagger_{b'}\hat{a}^\dagger_{a'}|0\rangle = -(a')^2\delta_{ab'}\delta_{bc'} + (a')^2\delta_{ab'}\delta_{cc'} + \\
+ (a')^2\delta_{ac'}\delta_{bb'} - (a')^2\delta_{ac'}\delta_{cb'} - (a')^2\delta_{bb'}\delta_{cc'} + (a')^2\delta_{bc'}\delta_{cb'} + (b')^2\delta_{aa'}\delta_{bc'} - (b')^2\delta_{aa'}\delta_{cc'} - \\
- (b')^2\delta_{ac'}\delta_{ba'} + (b')^2\delta_{ac'}\delta_{ca'} + (b')^2\delta_{ba'}\delta_{cc'} - (b')^2\delta_{bc'}\delta_{ca'} - (c')^2\delta_{aa'}\delta_{bb'} + (c')^2\delta_{aa'}\delta_{cb'} + \\
+ (c')^2\delta_{ab'}\delta_{ba'} - (c')^2\delta_{ab'}\delta_{ca'} - (c')^2\delta_{ba'}\delta_{cb'} + (c')^2\delta_{bb'}\delta_{ca'} - \delta_{aa'}\langle bc||b'c'\rangle + \delta_{ab'}\langle bc||a'c'\rangle - \\
- \delta_{ac'}\langle bc||a'b'\rangle + \delta_{ba'}\langle ac||b'c'\rangle - \delta_{bb'}\langle ac||a'c'\rangle + \delta_{bc'}\langle ac||a'b'\rangle - \delta_{ca'}\langle ab||b'c'\rangle + \delta_{cb'}\langle ab||a'c'\rangle - \\
- \delta_{cc'}\langle ab||a'b'\rangle
\end{aligned}
\tag{8}
$$

These and further tedious calculations were done using the second quantisation module from the SymPy [27] software library. Finally, the expansion coefficients C^{abc}_{nml} and energies of each eigenstate E_{nml} are obtained by diagonalizing this anti-symmetric matrix

$$
\hat{H}_{ED}|\psi_{nml}\rangle = E_{nml}|\psi_{nml}\rangle \tag{9}
$$

This is easily done using the *eigh* function, which is part of the linear algebra module of the SciPy [26] software library. While the only limiting factor, in terms of precision, is the truncation of the basis up to state n_{max}, it can be easily seen that the problem with this method is the exponentially increasing size of the Hilbert space for larger systems. For example, a system of 12 electrons with a basis size of 20 would already require $\frac{20!}{(20-12)!} \approx 60$TB of RAM to just store the matrix.

To analyze the probability distribution of a state, it is convenient to also calculate the one-particle transition density matrix

$$
\begin{aligned}
(\hat{\rho}_{nml\to n'm'l'})_{pq} \propto \sum_{abc}^{n_{max}}\sum_{a'b'c'}^{n_{max}} C^{abc}_{nml}C^{a'b'c'}_{n'm'l'}\langle 0|\hat{a}_a\hat{a}_b\hat{a}_c\hat{a}^\dagger_p\hat{a}_q\hat{a}^\dagger_{c'}\hat{a}^\dagger_{b'}\hat{a}^\dagger_{a'}|0\rangle = \sum_{abc}^{n_{max}}\sum_{a'b'c'}^{n_{max}} C^{abc}_{nml}C^{a'b'c'}_{n'm'l'}\times \\
\times(\delta_{pa}\delta_{qa'}\delta_{bb'}\delta_{cc'} - \delta_{pa}\delta_{qa'}\delta_{bc'}\delta_{cb'} - \delta_{pa}\delta_{qb'}\delta_{ba'}\delta_{cc'} + \delta_{pa}\delta_{qb'}\delta_{bc'}\delta_{ca'} + \delta_{pa}\delta_{qc'}\delta_{ba'}\delta_{cb'} - \\
- \delta_{pa}\delta_{qc'}\delta_{bb'}\delta_{ca'} - \delta_{pb}\delta_{qa'}\delta_{ab'}\delta_{cc'} + \delta_{pb}\delta_{qa'}\delta_{ac'}\delta_{cb'} + \delta_{pb}\delta_{qb'}\delta_{aa'}\delta_{cc'} - \delta_{pb}\delta_{qb'}\delta_{ac'}\delta_{ca'} - \\
- \delta_{pb}\delta_{qc'}\delta_{aa'}\delta_{cb'} + \delta_{pb}\delta_{qc'}\delta_{ab'}\delta_{ca'} + \delta_{pc}\delta_{qa'}\delta_{ab'}\delta_{bc'} - \delta_{pc}\delta_{qa'}\delta_{ac'}\delta_{bb'} - \delta_{pc}\delta_{qb'}\delta_{aa'}\delta_{bc'} + \\
+ \delta_{pc}\delta_{qb'}\delta_{ac'}\delta_{ba'} + \delta_{pc}\delta_{qc'}\delta_{aa'}\delta_{bb'} - \delta_{pc}\delta_{qc'}\delta_{ab'}\delta_{ba'})
\end{aligned}
\tag{10}
$$

Consequently, the probability distribution for a state with quantisation numbers nml is obtained via the single particle basis functions

$$
\rho_{nml}(x) \propto \sum_{ij}(\hat{\rho}_{nml\to nml})_{ij}\langle\psi_i|x\rangle\langle\psi_j|x\rangle \tag{11}
$$

An interesting quantity, that describes how the system interacts with EM radiation, is the absorption spectrum, which can be obtained via scattering theory [28]

$$I(E) \propto \Im\left(\sum_{abc} \frac{|\langle\psi_{123}|\hat{d}|\psi_{abc}\rangle|^2}{E-(E_{abc}-E_{123})+i\eta}\right) = \Im\left(\sum_{abc} \frac{|\,\mathsf{Tr}(\hat{\rho}_{123\to abc}\hat{d})|^2}{E-(E_{abc}-E_{123})+i\eta}\right) \tag{12}$$

Here $\eta \ll 1$ is arbitrary, accounting for the finite lifetime of a state, and $\hat{d} \propto \hat{x}$ is the dipole operator

$$\hat{d}_{pq} = \langle p|\hat{x}|q\rangle \propto \int_0^\pi \sin(px)x\sin(qx)dx = 2pq\frac{(-1)^{p+q}-1}{(p^2-q^2)^2} \tag{13}$$

2.2.2 Coupled Cluster

Coupled cluster [29] expands the ground state solution $|\Psi\rangle$ on the basis set via an exponential excitation operator $\hat{T}$

$$|\Psi\rangle = e^{\hat{T}}|\Psi_0\rangle \tag{14}$$

Here $|\Psi_0\rangle$ is the non-interacting solution, expressed in terms of the single particle basis described previously, but can also be a previous Hartree-Fock or other simulation, with the respective operator algebra, to speed up convergence. This exponential approach enables size-extensivity and thus $\hat{T}$ can be truncated to only include singles (CCS), singles and doubles (CCSD) and further on, allowing to choose between precision and performance

$$\hat{T} = \sum_{a,a'}^{n_{max}} t_{a\to a'}\hat{a}^\dagger_{a'}\hat{a}_a + \frac{1}{4}\sum_{ab,a'b'}^{n_{max}} t_{ab\to a'b'}\hat{a}^\dagger_{a'}\hat{a}^\dagger_{b'}\hat{a}_b\hat{a}_a + \dots \tag{15}$$

It should be clear that the only contributions will be where $\{abc\dots\}$ corresponds to occupied states and $\{a'b'c'\dots\}$ to the remaining, or so called virtual, states. In practice CCSD(T) is usually enough for most high precision simulations, but in this chapter CCSD will be used for a qualitative picture. The amplitudes $\{t_{abc\dots\to a'b'c'\dots}\}$ are found by imposing

$$\begin{aligned}\langle\psi_0|\hat{a}^\dagger_{a'}\hat{a}_a e^{-\hat{T}}\hat{H}e^{\hat{T}}|\psi_0\rangle &= 0\\ \langle\psi_0|\hat{a}^\dagger_{a'}\hat{a}^\dagger_{b'}\hat{a}_a\hat{a}_b e^{-\hat{T}}\hat{H}e^{\hat{T}}|\psi_0\rangle &= 0\\ \dots\end{aligned} \tag{16}$$

The resulting equations were derived by using the pdaggerq [30] software library, which also transforms them into Python functions utilizing the efficient *einsum* function from the NumPy [31] software library. The foundation of pdaggerq uses properties of the fermion operators and the Baker–Campbell–Hausdorff formula to evaluate these types of expressions

$$e^{-\hat{A}}\hat{B}e^{\hat{A}} = \hat{B} + [\hat{A},\hat{B}] + \frac{1}{2!}[\hat{A},[\hat{A},\hat{B}]] + \frac{1}{3!}[\hat{A},[\hat{A},[\hat{A},\hat{B}]]] + \ldots \tag{17}$$

The numerical solution can be calculated by using the *root* function, part of the SciPy software library. Specifically, it has been shown [32] that Krylov solvers are particularly suitable for these large equation sets, since they don't require evaluation and storage of the entire Jacobian. A helpful tactic is to build-up from a known solution, for example, at $L = 0$ the potential vanishes and thus all of the amplitudes are zero. Slowly increasing the separation and using extrapolated values from previous simulations as an initial guess can accelerate convergence.

While the ground state energy can be calculated from $E = \langle\psi_0|e^{-\hat{T}}\hat{H}e^{\hat{T}}|\psi_0\rangle$ and its properties from a slight modification, the more general equation of motion (EOM) framework [33] enables evaluation of energies and properties of every state. This involves adding a non-Hermitian excitation operator (like in Eq. 15) to the ground state wavefunction

$$\begin{aligned} |\psi_{\{m_i\}}\rangle &= \hat{R}_{\{m_i\}}e^{\hat{T}}|\psi_0\rangle \\ \langle\psi_{\{m_i\}}| &= \langle\psi_0|e^{-\hat{T}}\hat{L}_{\{m_i\}} \end{aligned} \tag{18}$$

After some simple manipulation, this can be rewritten as an eigenvalue problem

$$\begin{aligned} \mathcal{H}\hat{R}_{\{m_i\}}|\psi_0\rangle &= E_{\{m_i\}}\hat{R}_{\{m_i\}}|\psi_0\rangle \\ \langle\psi_0|\hat{L}_{\{m_i\}}\mathcal{H} &= \langle\psi_0|\hat{L}_{\{m_i\}}E_{\{m_i\}} \end{aligned} \tag{19}$$

Here $\mathcal{H} = e^{-\hat{T}}\hat{H}e^{\hat{T}}$ is the similarity transformed Hamiltonian and, unlike the full Hamiltonian in Eq. 5, contains numerous many-body terms, thus requiring the same truncation technique as for the excitation operators previously. The similarity transformed Hamiltonian can be obtained as before, by using the pdaggerq library, after separating it into blocks of different order many-body operators. The left and right eigenvectors, eigenvalues can be calculated using the *eig* function of the SciPy software library.

In addition to the state energies $E_{\{m_i\}}$, the eigenvectors of $\hat{L}_{\{m_i\}}$ and $\hat{R}_{\{m_i\}}$ can be used to derive the one-particle density matrix. Furthermore, its non-Hermitian nature results in a slight change to the intensity of the absorption spectrum, described by Eq. 12

$$|\langle\psi_{\{m_0\}}|\hat{d}|\psi_{\{m_i\}}\rangle|^2 \rightarrow |\,\mathsf{Tr}(\hat{\rho}_{\{m_0\}\rightarrow\{m_i\}}\hat{d})\,\mathsf{Tr}(\hat{\rho}_{\{m_i\}\rightarrow\{m_0\}}\hat{d})| \tag{20}$$

A more complete description of this type - the extended coupled cluster formalism - will be introduced in the next section.

2.2.3 Hartree-Fock

The Hartree-Fock method [34] approximates a N particle ground state wavefunction as a product of anti-symmetrized single-particle wavefunctions, also known as a Slater determinant, which in turn are formed as a linear superposition of the basis

$$\langle \psi_{\{m_0\}} | x_1, x_2, \ldots, x_N \rangle \approx \mathcal{A} \prod_{i=1}^{N} \langle \Psi_i | x_i \rangle = \mathcal{A}_\alpha \prod_{i=1}^{N} \left[\sum_{j=1}^{n_{max}} C_{ij} \langle \psi_i | x_i \rangle \right]_\alpha \tag{21}$$

Sequentially, Hartree-Fock is known to neglect correlation effects, but is still relatively precise for a large variety of systems. A very similar procedure to the equation of motion framework, called the random-phase approximation, is used to describe excited states, but will not be detailed here.

Simple use of Lagrangian multipliers to minimize the energy, meanwhile preserving normalisation, yields a self-consistent eigenvalue equation

$$\hat{F} C_i = \epsilon_i C_i \tag{22}$$

Given an initial guess, this equation is solved iteratively with the new coefficients used to update the Fock matrix containing the one-particle and two-particle terms, discussed previously

$$\hat{F}_{pq} = \delta_{pq} p^2 + \frac{1}{2} \sum_{rs}^{n_{max}} \hat{\rho}_{rs} \langle pr || qs \rangle \tag{23}$$

Here $\hat{\rho}$ is the one-particle density matrix

$$\hat{\rho}_{pq} = \sum_{n=1}^{N} C_{np} C_{nq} \tag{24}$$

As before in Eq. 11, this quantity can be used to look at the probability distribution of the system. The ground state energy is calculated after each iteration and the simulation is stopped once the relative difference between sequential runs reaches the desired magnitude

$$E = \sum_{p} \hat{\rho}_{pp} p^2 + \frac{1}{2} \sum_{pqrs} \hat{\rho}_{pr} \hat{\rho}_{qs} \langle pq || rs \rangle \tag{25}$$

As mentioned earlier, to ease convergence it is possible to start from a known solution and slowly build up to the required one, whilst extrapolating from previous simulations to form sequential initial guesses.

2.3 Numerical Simulations

2.3.1 The case of 3 Electrons

Simulations for three boxed electrons were run for each of the methods mentioned above. It is initially useful to look at the convergence of the Hartree-Fock simulation, displayed in Fig. 1 for different box length L values. The colored quantity is the order of magnitude of relative differences between sequential measurements. Note that 10^{-16} is the precision limit in Python for 64 bit floating point numbers. As expected, larger box lengths require more iterations for convergence, because of the increased role of electrostatic interactions. It can be also concluded that around 10 iterations is already enough to produce reasonable accuracy.

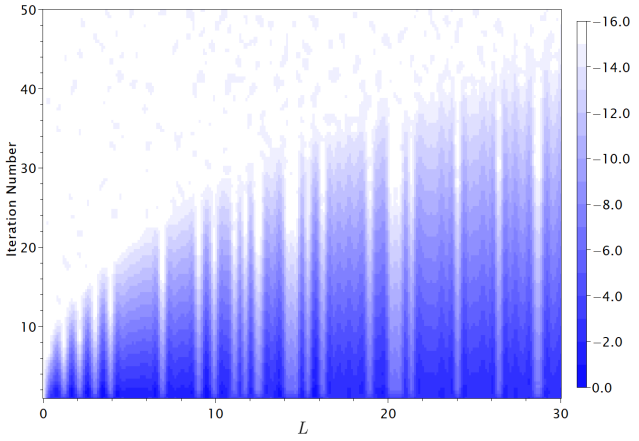

Fig. 1. The convergence of a Hartree-Fock simulation for 3 boxed electrons with respect to the box length and iteration number. The colored quantity is the order of magnitude of the relative difference between sequential simulations.

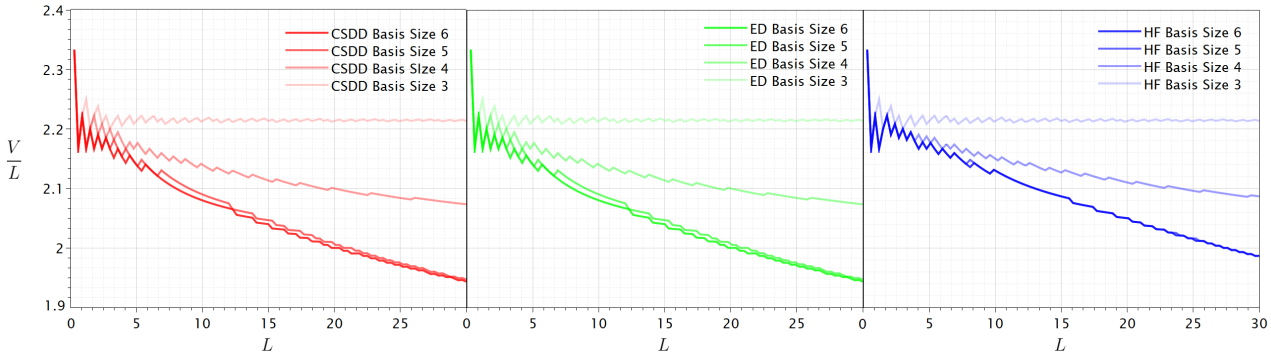

Fig. 2. The convergence of coupled cluster, exact diagonalization and Hartree-Fock electrostatic energies per box length for three boxed electrons. Length and energy scales are expressed in terms of Bohr radii a_0 and ground state energies of a single trapped electron, respectively.

Further, the convergence of the ground state electrostatic energy per box length is displayed in Fig. 2. It is immediately visible that for a qualitative picture a sin function basis size of 6 is more than satisfactory. The graphs reveal that Hartree-Fock produces a slight overestimate as well, which is caused by the neglect of correlation effects.

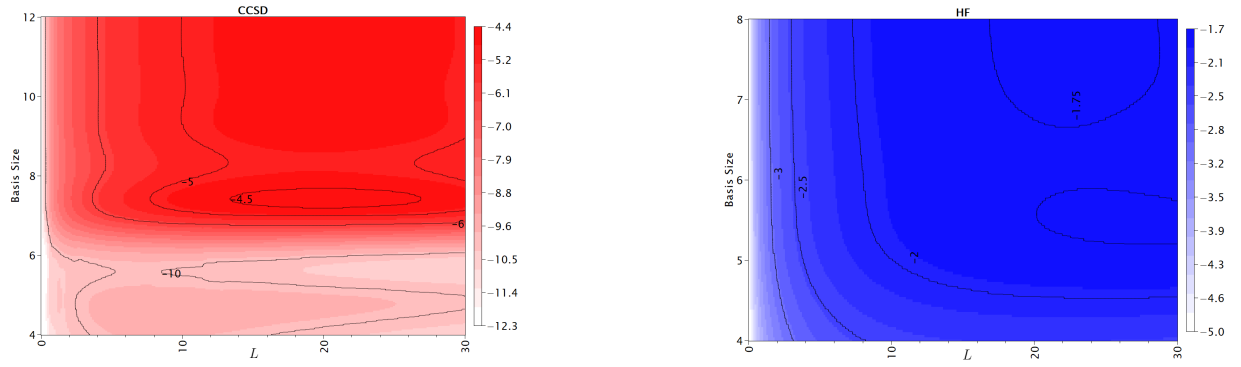

Fig. 3. Relative ground state energy deviations, when comparing Hartree-Fock and coupled cluster simulations with exact diagonalization as the reference. The order of magnitude of this quantity with respect to box length and basis size is shown.

A more quantitative analysis of Hartree-Fock and coupled cluster deviations from exact diagonalization is displayed in Fig. 3. The colored quantities are the orders of magnitude of relative differences with respect to box length and basis size. Whilst coupled cluster initially closely follows exact diagonalization, it converges to an error of magnitude approximately 10^{-4}. It is most probable that, as the correlation effects increase, the neglect of higher orders of coupled cluster excitations becomes more pronounced. At the same time Hartree-Fock consistently produces an error of a few percent, because of the neglect of all correlation.

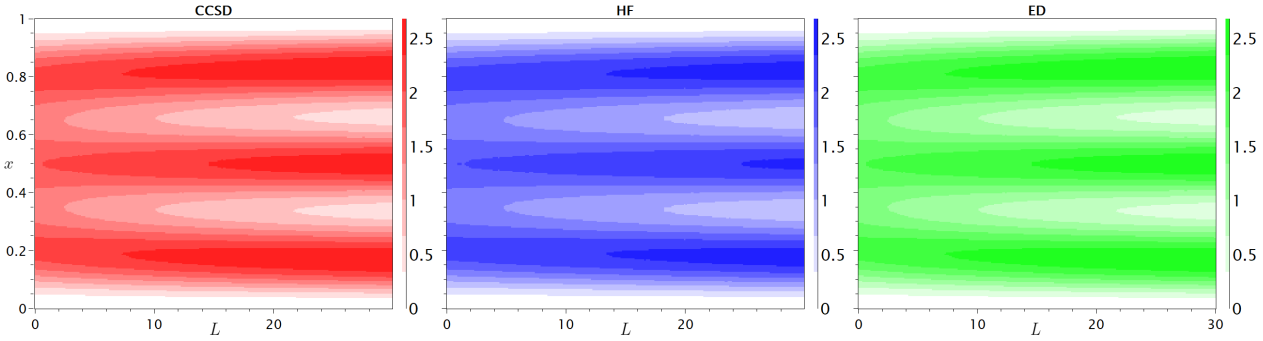

Fig. 4. The ground state probability densities of coupled cluster, exact diagonalization and Hartree-Fock simulations for three boxed electrons. The x coordinate is expressed in terms of the box length L, which in turn is expressed in terms of Bohr radii.

Moving on now to consider other ground state observables, the probability density for all three simulations is displayed in Fig. 4. The x coordinate is expressed in terms of the box length L. Neglect of correlation effects again stands out, as a small difference for Hartree-Fock is visible at at the first few L. Nevertheless, the accuracy of the ground state energy curves translates well into ground state observables.

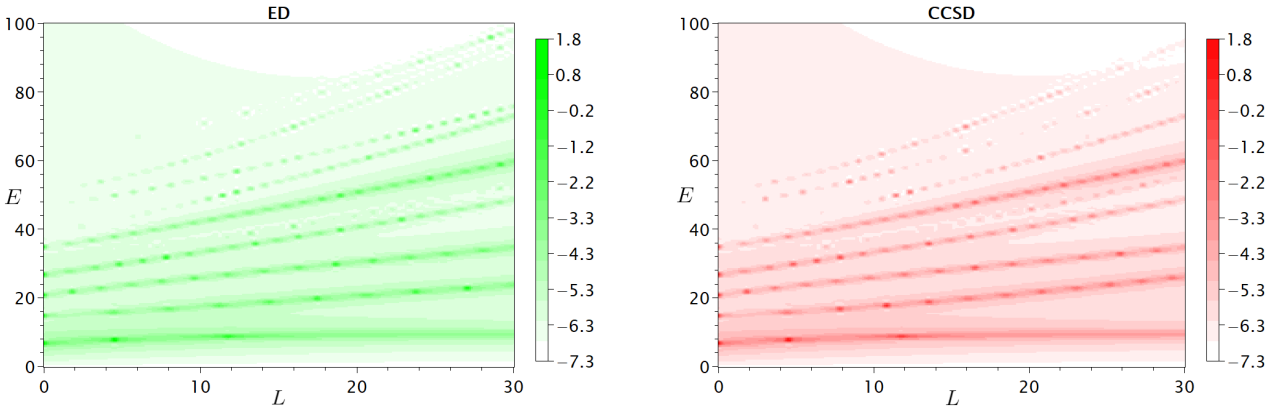

Fig. 5. The EM absorption spectrum of a three boxed particle system from exact diagonalization and coupled cluster simulations. The colored quantity represents the order of magnitude of the absorption spectrum intensity, with respect to the box length and energy of the inbound photon.

Because the expectation of the particle number is conserved in coupled cluster and is thus known, it is proposed that this property of the density matrix can serve as a rough estimate of the accuracy of a coupled cluster solution

$$\lim_{n_{max}\to\infty} \mathrm{Tr}(\rho_{\{m_i\}\to\{m_i\}}) = N \qquad (26)$$

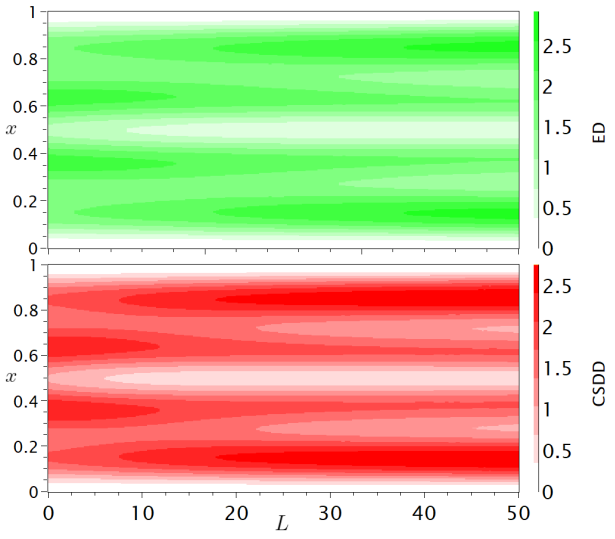

Fig. 6. The probability density of the first excited state of the three boxed electron system from exact diagonalization and coupled cluster simulations. The x coordinate is expressed in terms of the box length L, which in turn is expressed in terms of Bohr radii.

Finally, the application of coupled cluster and exact diagonalization is compared for excited states. In Fig. 5 the resulting order of magnitude of the absorption spectrum intensity from Eq. 12 is displayed as a function of the box length and energy of the inbound photon with $\eta \sim 10^{-3}$ decay width energy. As expected, higher-energy excitations deviate more from the exact diagonalization reference. Nevertheless, the qualitative agreement is quite good, even for excited states. Furthermore, looking at the probability density of the first excited state, displayed in Fig. 6, confirms this. Finally, it was observed that the particle number deviated at an average of 3% over all states, thus giving at least some confidence in the observations for coupled cluster in this subsection.

2.3.2 The case of 15 Electrons

In this subsection brief results are presented for Hartree-Fock and coupled cluster simulations in the case of 15 particles. It was found that a basis size of 24 is enough for a qualitative picture, de-

fined the same as in the previous section.

In the case of Hartree-Fock, 10 iterations produced a more than satisfactory final relative difference of less than 10^{-6}. For coupled cluster, the particle number deviated no more than 3% as with the 3 particle case. In Fig. 7 the relative difference of the ground state energy between both simulations is displayed. A divergent growth can be observed, reaching an order of 1% for a dilute gas. One-particle density matrices are not displayed here due to the amount of particles, but exhibit the same dynamics as for the 3 particle case. Finally, the absorption spectrum for this system is displayed in Fig. 8.

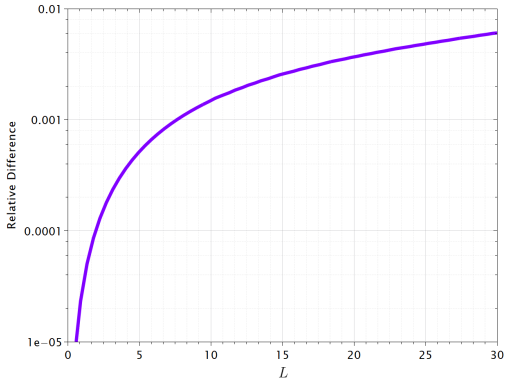

Fig. 7. Relative energy difference of the ground state energy between Hartree-Fock and coupled cluster simulations for the case of 15 particles.

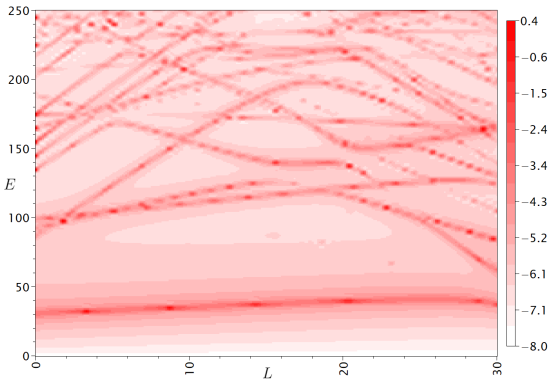

Fig. 8. The absorption spectrum as simulated from a coupled cluster calculation for the case of 15 particles.

As expected, the absorption spectrum is now much more complex, because of the larger amount of particles. While, as mentioned before, the particle number conservation property deviated no more than 3% for the states visible in this spectra, higher excitations produced very large relative deviations of around $\sim 10^1$ and thus were unreliable. It is expected that this is because of the applied truncation for EOM, only including singles and doubles, with similar behaviour seen in the previous subsection with ground state properties.

3 Study of Correlation Effects in Single Layer Graphene

In this section the extended coupled cluster equations are derived using the particle-hole formalism at doubles truncation. This method is then applied to examine the electrostatic and correlation effects present in single layer graphene. A nearest neighbour hopping model is used with an addition of a electrostatic potential, calculated via Ewald summation to account for the periodicity. Energies, band structures and chemical potentials are reported for integer fillings of opposite sign. Automatic differentiation is introduced as a way to run simulations in this framework.

3.1 Application of Ewald Summation to the Periodic Lattice

A single graphene sheet is formed of infinite periodic, rhombic unit cells, displayed in Fig. 9. Therefore Ewald summation [35] is used to rapidly calculate the electrostatic potential from a point charge and its copies, distance **r** away. In contrast, a direct calculation in real space would be slowly convergent. In two dimensions, this potential is defined [36] for a neutral system by a rapidly converging short range and long range term

$$V(\mathbf{r}) \propto \sum_{\mathbf{x}} \frac{1-\delta_{\mathbf{r},\mathbf{0}}}{|\mathbf{r}-\mathbf{x}|}\mathrm{erfc}\left(\frac{|\mathbf{r}-\mathbf{x}|}{2\eta}\right) - \frac{\delta_{\mathbf{r},\mathbf{0}}}{\sqrt{\pi}\eta} - \frac{2\pi}{|\mathbf{a_1}\times\mathbf{a_2}|}\left[r_z\mathrm{erfc}\left(\frac{r_z}{2\eta}\right) + \frac{2\eta}{\sqrt{\pi}}e^{-\frac{r_z^2}{4\eta^2}}\right] + \\ + \frac{\pi}{|\mathbf{a_1}\times\mathbf{a_2}|}\sum_{\mathbf{k}\neq\mathbf{0}}\frac{\cos(k_x r_x + k_y r_y)}{|\mathbf{k}|}\left[e^{|\mathbf{k}||r_z|}\mathrm{erfc}\left(|\mathbf{k}|\eta + \frac{|r_z|}{2\eta}\right) + e^{-|\mathbf{k}||r_z|}\mathrm{erfc}\left(|\mathbf{k}|\eta - \frac{|r_z|}{2\eta}\right)\right] \tag{27}$$

Here the lattice unit vectors $\mathbf{a_1} = \frac{a}{2}(3,\sqrt{3})$ and $\mathbf{a_2} = \frac{a}{2}(3,-\sqrt{3})$ and the reciprocal lattice vectors $\mathbf{g_1} = \frac{2\pi}{3}(1,\sqrt{3})$ and $\mathbf{g_2} = \frac{2\pi}{3a}(1,-\sqrt{3a})$ are used for particle sampling in the sums via

$$\begin{aligned} \mathbf{x} &= n_1\mathbf{a_1} + n_2\mathbf{a_2} \qquad & n_1, n_2 \in [-N, N] \\ \mathbf{k} &= m_1\mathbf{g_1} + m_2\mathbf{g_2} \qquad & m_1, m_2 \in [-N, N] \end{aligned} \tag{28}$$

To simplify the algebra, length and energy scales in further sections are expressed in terms of the lattice constant a and the hopping constant t respectively. These and other parameters for graphene were taken from a first-principles calculation [37] leading to a proportionality constant of $0.87t$ in the potential relation above and a Hubbard term of $U = 3.3t$.

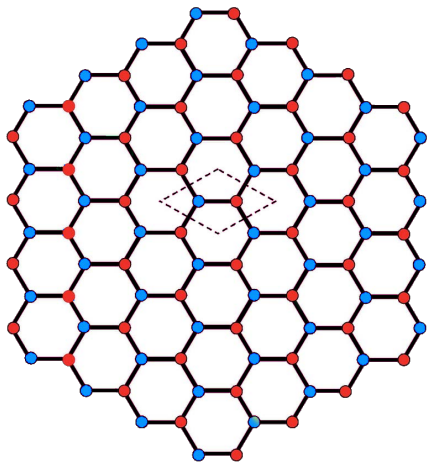

Fig. 9. Geometric structure of a single graphene sheet. The rhombic unit cell is outlined.

For single layer graphene there is no three dimensional dependence and thus r_z can be set to zero.

While the parameter η is arbitrary, it is to be chosen so that convergence is achieved with a minimal value of N. The suggested estimate $\eta \approx 0.1|\mathbf{a_1} \times \mathbf{a_2}|^{\frac{1}{2}} = 0.3a$ was used for single layer graphene calculations and, as an example, the four cases of interest are computed here.

The first concerns a charge neutral unit cell - one positive and one negative charge of distance $\mathbf{r} = (\pm a, 0)$ apart. This potential is easily computed from the above formula, combining contributions from the images of the charge itself $V(\mathbf{0})$ and of the other one and its images $V(\mathbf{r})$, producing $V_{\pm,\mp}(\mathbf{r}) = -1.34t$. This result converged with $N = 1$ and any substantial changes in η produced the same value, but required larger values of N.

The second case concerns the same system, but now with two charges of the same sign. Since the above formula is only valid for a charged system, the Widom insertion method [38] is applied here to calculate this value. In the first approximation, another positive point charge of double magnitude is inserted on top of the negative one in the system discussed above. The resulting expression is obtained as $V_{\pm,\pm}(\mathbf{r}) = -V_{\pm,\mp}(\mathbf{r}) = 1.34t$. In the second approximation, this is done together with a uniformly charged background to make the system neutral. The effects of this background are then removed to produced the final value. While this may be significant for other systems with weaker electrostatic interactions, it was found that this correction produced a negative shift of around 1%. Finally, it can be easily deduced that $V_{\pm,\mp}(\mathbf{0}) = 0$ and using the same method produces $V_{\pm,\pm}(\mathbf{0}) = 4.2t$.

3.2 Description via Extended Coupled Cluster

It has been shown [39] that the non-interacting electron gas in a sheet of graphene is well modelled via a nearest neighbor hopping interaction, denoted by $\langle \mathbf{r_1}, \mathbf{r_2} \rangle$ within the negative and positive energy bands $n = \{\pm\}$. The electrostatic interaction can easily be added to this description and results in the following Hamiltonian in coordinate space

$$\hat{H} = \sum_{\langle \mathbf{r_1}, \mathbf{r_2} \rangle, n} \epsilon_{\mathbf{r_1}, \mathbf{r_2}, n} \, \hat{d}^{\dagger}_{\mathbf{r_1}, n} \hat{d}_{\mathbf{r_2}, n} + \frac{1}{2} \sum_{\langle \mathbf{r_1}, \mathbf{r_2} \rangle, n_1, n_2} V_{n_1, n_2}(\mathbf{r_2} - \mathbf{r_1}) \, \hat{n}_{\mathbf{r_1}, n_1} \hat{n}_{\mathbf{r_2}, n_2} \tag{29}$$

In the following expressions, explicit summation will be removed by using the Einstein summation convention. This expression is then transformed into momentum space to expose the non-interacting bands and Fourier transformed, anti-symmetric elements of the electrostatic potential

$$\begin{aligned} \hat{H} = \frac{\Delta_{\mathbf{k}} \hat{n}_{\mathbf{k},+} - \Delta_{\mathbf{k}} \hat{n}_{\mathbf{k},-}}{N_0} + \\ + \frac{\delta_{n_1,n_4} \delta_{n_2,n_3} \delta_{\mathbf{k_1}+\mathbf{k_2},\mathbf{k_3}+\mathbf{k_4}}}{2N_0^3} [V_{n_1,n_3}(\mathbf{k_2} - \mathbf{k_3}) - V_{n_1,n_3}(\mathbf{k_1} - \mathbf{k_3})] \, \hat{d}^{\dagger}_{\mathbf{k_1}, n_1} \hat{d}_{\mathbf{k_4}, n_4} \hat{d}^{\dagger}_{\mathbf{k_2}, n_2} \hat{d}_{\mathbf{k_3}, n_3} \end{aligned} \tag{30}$$

Here the real potential in momentum space is expressed as

$$V_{n_1,n_2}(\mathbf{k}) = \sum_{\mathbf{r_1},\mathbf{r_2}} V_{n_1,n_2}(\mathbf{r_2} - \mathbf{r_1})\ \cos(\mathbf{k} \cdot (\mathbf{r_2} - \mathbf{r_1})) \tag{31}$$

Because the Fourier transform is done over the first Brillouin zone, such is the summation in the equation above. This results in the fact that for single layer graphene, only the four values, calculated in the previous subsection, of the potential are required for single layer graphene. The Hubbard term is included in $V_{\pm,\pm}(\mathbf{0})$ as well.

The momentum values are sampled with a Monkhorst-Pack grid [40] for hexagonal lattices [41]

$$\mathbf{k} = \frac{n_1}{N_k}\mathbf{b_1} + \frac{n_2}{N_k}\mathbf{b_2} \qquad n_1 < n_2 \in [0, N_k) \tag{32}$$

In further calculations N_0 represents the resulting total amount of momentum sampling points. Due to the quadruple symmetry, present in this grid for single layer graphene, the 1st Brillouin zone can be split into four identical parts and thus the computational cost can be reduced by sampling only one of these regions. Simple geometric analysis reveals that this can be accomplished by using $\mathbf{b_1} = \frac{\mathbf{g}_1+\mathbf{g}_2}{2}$, $\mathbf{b_2} = \frac{\mathbf{g}_1-\mathbf{g}_2}{2}$.

Moving on, the operator indexation is generalized a bit and compressed to simplify the upcoming tedious calculations

$$\hat{H} = \epsilon_{\mathbf{k},n}\hat{n}_{\mathbf{k},n} + \frac{1}{2}V_{\mathbf{k_1},n_1,\mathbf{k_2},n_2,\mathbf{k_3},n_3,\mathbf{k_4},n_4}\hat{d}^\dagger_{\mathbf{k_1},n_1}\hat{d}_{\mathbf{k_4},n_4}\hat{d}^\dagger_{\mathbf{k_2},n_2}\hat{d}_{\mathbf{k_3},n_3} = \epsilon_{ij}\hat{d}^\dagger_i\hat{d}_j + \frac{1}{2}V_{ijkl}\hat{d}^\dagger_i\hat{d}_l\hat{d}^\dagger_j\hat{d}_k \tag{33}$$

Because of the phase transitions present in the system explored in the next section, along with strong correlations, extended coupled cluster [6], of which normal coupled cluster is a subset, will be used instead. The standard occupied-virtual particle formalism, used in the previous section, leads to very complex algebra and thus a particle-hole formalism is utilized instead, in which the excitation operators are made from only creation operators. The reference vacuum is also shifted to the half-filled ground state, where the negative energy band is filled and the positive one is empty. This is controlled by the number operator and it is important to note that mathematically the vacuum is empty. The extended coupled cluster singles and doubles (ECCSD) excitation operators are then defined as

$$\hat{T} = t_{\mathbf{k_1}n_1,\mathbf{k_2}n_2}\hat{d}^\dagger_{\mathbf{k_1}n_1}\hat{d}^\dagger_{\mathbf{k_2}n_2} + t_{\mathbf{k_1}n_1,\mathbf{k_2}n_2,\mathbf{k_3}n_3,\mathbf{k_4}n_4}\hat{d}^\dagger_{\mathbf{k_1}n_1}\hat{d}^\dagger_{\mathbf{k_2}n_2}\hat{d}^\dagger_{\mathbf{k_3}n_3}\hat{d}^\dagger_{\mathbf{k_4}n_4} = \frac{1}{2!}t_{ij}\hat{d}^\dagger_i\hat{d}^\dagger_j + \frac{1}{4!}t_{ijkl}\hat{d}^\dagger_i\hat{d}^\dagger_j\hat{d}^\dagger_k\hat{d}^\dagger_l \tag{34}$$

Additionally, the main object of interest has now become more complicated with $e^{-\hat{T}}\hat{H}e^{\hat{T}} \rightarrow e^{\hat{T}'}e^{-\hat{T}}\hat{H}e^{\hat{T}}$. Here the excitation operator $\hat{T}'$ is the same as $\hat{T}$, but with its own coefficients and

annihilation operators instead of creation ones. To symbolically evaluate and simplify these tedious expressions, custom Mathematica [42] software was written up and utilized, as other packages failed to produce the correct expressions and simplification for this formalism. Initially, it is important to evaluate

$$
\begin{aligned}
e^{-\hat{T}}\hat{H}e^{\hat{T}} = \epsilon_{ij}\hat{d}_i^\dagger\hat{d}_j + \frac{1}{2}V_{ijkl}\hat{d}_i^\dagger\hat{d}_l\hat{d}_j^\dagger\hat{d}_k + \frac{1}{2}(V_{ikkl}t_{jl} - V_{ijkl}t_{kl} - 2\epsilon_{ik}t_{jk})\hat{d}_i^\dagger\hat{d}_j^\dagger + \\
+ V_{ijlm}t_{km}\hat{d}_i^\dagger\hat{d}_j^\dagger\hat{d}_k^\dagger\hat{d}_l - \frac{1}{12}(V_{immn}t_{njkl} + 3V_{ijmn}t_{mnkl})\hat{d}_i^\dagger\hat{d}_j^\dagger\hat{d}_k^\dagger\hat{d}_l^\dagger + \frac{1}{2}V_{ijmn}t_{km}t_{ln}\hat{d}_i^\dagger\hat{d}_j^\dagger\hat{d}_k^\dagger\hat{d}_l^\dagger + \\
+ \frac{1}{6}\epsilon_{im}t_{mjkl}\hat{d}_i^\dagger\hat{d}_j^\dagger\hat{d}_k^\dagger\hat{d}_l^\dagger - \frac{1}{6}V_{ijno}t_{oklm}\hat{d}_i^\dagger\hat{d}_j^\dagger\hat{d}_k^\dagger\hat{d}_l^\dagger\hat{d}_m^\dagger\hat{d}_n + \frac{1}{6}V_{ijop}t_{ok}t_{plmn}\hat{d}_i^\dagger\hat{d}_j^\dagger\hat{d}_k^\dagger\hat{d}_l^\dagger\hat{d}_m^\dagger\hat{d}_n^\dagger + \\
+ \frac{1}{72}V_{ijrs}t_{rklm}t_{snop}\hat{d}_i^\dagger\hat{d}_j^\dagger\hat{d}_k^\dagger\hat{d}_l^\dagger\hat{d}_m^\dagger\hat{d}_n^\dagger\hat{d}_o^\dagger\hat{d}_p^\dagger
\end{aligned}
\tag{35}
$$

Further, the object $e^{\hat{T}'}$ must be evaluated with the previous equation in mind, because, in its standalone form, it is an infinite series of operators. Therefore, only terms with a maximum of 8 annihilation operators should be kept

$$
\begin{aligned}
e^{\hat{T}'} = 1 + \frac{1}{2}t'_{ij}\hat{d}_i\hat{d}_j + \frac{1}{24}\left(t'_{ijkl} + 3t'_{ij}t'_{kl}\right)\hat{d}_i\hat{d}_j\hat{d}_k\hat{d}_l + \frac{1}{48}\left(t'_{ij}t'_{klmn} + t'_{ij}t'_{kl}t'_{mn}\right)\hat{d}_i\hat{d}_j\hat{d}_k\hat{d}_l\hat{d}_m\hat{d}_n + \\
+ \frac{1}{1152}\left(t'_{ijkl}t'_{mnop} + 3t'_{ij}t'_{kl}t'_{mn}t'_{op} + 6t'_{ij}t'_{kl}t'_{mnop}\right)\hat{d}_i\hat{d}_j\hat{d}_k\hat{d}_l\hat{d}_m\hat{d}_n\hat{d}_o\hat{d}_p
\end{aligned}
\tag{36}
$$

Further, all of these expressions are combined and simplified to obtain the ECCSD energy equation. This was done with some help of the second quantisation module in the Sympy software library as well as a custom parser that converts these tensor operations in terms of *einsum* functions from the NumPy software library. Thus the following energy equation is obtained

$$
\begin{aligned}
E = \langle -|e^{\hat{T}'} e^{-\hat{T}} \hat{H} e^{\hat{T}}|-\rangle = \epsilon_{ik} t_{jk} t'_{ij} + \frac{1}{2} V_{ijkl} t'_{ij} t_{kl} - \frac{1}{2} V_{ikkl} t'_{ij} t_{jl} + \\
+ \frac{1}{2} V_{ijmn} t_{km} t_{ln} (t'_{ij} t'_{kl} - 2 t'_{ik} t'_{jl} + t'_{ijkl}) + \frac{1}{12} V_{immn} t_{jkln} (t'_{ijkl} - 3 t'_{ik} t'_{jl}) + \\
+ \frac{1}{4} V_{ijmn} t_{klmn} (2 t'_{ik} t'_{jl} - t'_{ij} t'_{kl} - t'_{ijkl}) - \frac{1}{6} \epsilon_{im} t_{jklm} (t'_{ijkl} - 3 t'_{ik} t'_{jl}) + \\
+ \frac{1}{6} V_{ijop} t_{ko} t_{lmnp} (2 t'_{ik} t'_{jlmn} + 6 t'_{im} t'_{jkln} + 3 t'_{km} t'_{ijln} - 3 t'_{mn} t'_{ijkl} - t'_{ij} t'_{klmn} + \\
+ 3 t'_{ij} t'_{km} t'_{ln} + 6 t'_{ik} t'_{jl} t'_{mn} + 6 t'_{il} t'_{jm} t'_{kn}) + \frac{1}{72} V_{ijrs} t_{klmr} t_{nops} (6 t'_{ijkl} t'_{mnop} + 9 t'_{ijkn} t'_{lmop} - \\
- 18 t'_{imop} t'_{jkln} - 2 t'_{iklm} t'_{jnop} + 6 t'_{ij} t'_{kl} t'_{nops} + 9 t'_{ij} t'_{kn} t'_{lmop} + 12 t'_{ik} t'_{jm} t'_{lnop} + \\
+ 18 t'_{ik} t'_{jo} t'_{lmnp} + 72 t'_{ik} t'_{ln} t'_{jmop} + 36 t'_{ik} t'_{np} t'_{jlmo} + 12 t'_{il} t'_{km} t'_{knop} - 18 t'_{mo} t'_{np} t'_{ijkl} - \\
- 18 t'_{lp} t'_{mn} t'_{ijko} - 9 t'_{lm} t'_{np} t'_{ijko} + 9 t'_{ij} t'_{kl} t'_{mn} t'_{op} + 6 t'_{ij} t'_{kn} t'_{lp} t'_{mo} + 36 t'_{ik} t'_{jl} t'_{mo} t'_{np} + \\
+ 36 t'_{ik} t'_{jn} t'_{lo} t'_{mp} + 18 t'_{ik} t'_{jo} t'_{lm} t'_{np})
\end{aligned}
\tag{37}
$$

Note that this expression gives the energy difference from the half-filling state. Further, this equation can be reduced by contracting some summations over doubles and singles to just singles. For example, a term containing $t_{klmr} t'_{kl}$ can be absorbed to singles and thus removed, if $\{k, l\}$ don't appear anywhere else in it. Consequently, the final expression for the ECCSD energy is obtained as

$$
\begin{aligned}
E = \langle -|e^{\hat{T}'} e^{-\hat{T}} \hat{H} e^{\hat{T}}|-\rangle = \epsilon_{ik} t_{jk} t'_{ij} + \frac{1}{2} V_{ijkl} t'_{ij} t_{kl} - \frac{1}{2} V_{ikkl} t'_{ij} t_{jl} + \\
+ \frac{1}{2} V_{ijmn} t_{km} t_{ln} (t'_{ij} t'_{kl} - 2 t'_{ik} t'_{jl} + t'_{ijkl}) + \frac{1}{12} V_{immn} t_{jkln} t'_{ijkl} + \frac{1}{4} V_{ijmn} t_{klmn} (2 t'_{ik} t'_{jl} - t'_{ijkl}) - \\
- \frac{1}{6} \epsilon_{im} t_{jklm} t'_{ijkl} + \frac{1}{6} V_{ijop} t_{ko} t_{lmnp} (2 t'_{ik} t'_{jlmn} + 6 t'_{im} t'_{jkln} + 3 t'_{km} t'_{ijln} - t'_{ij} t'_{klmn} + 6 t'_{il} t'_{jm} t'_{kn}) + \\
+ \frac{1}{72} V_{ijrs} t_{klmr} t_{nops} (6 t'_{ijkl} t'_{mnop} + 9 t'_{ijkn} t'_{lmop} - 18 t'_{imop} t'_{jkln} - 2 t'_{iklm} t'_{jnop} + 9 t'_{ij} t'_{kn} t'_{lmop} + \\
+ 12 t'_{ik} t'_{jm} t'_{lnop} + 18 t'_{ik} t'_{jo} t'_{lmnp} + 72 t'_{ik} t'_{ln} t'_{jmop} - 18 t'_{lp} t'_{mn} t'_{ijko} + 6 t'_{ij} t'_{kn} t'_{lp} t'_{mo} + \\
+ 36 t'_{ik} t'_{jn} t'_{lo} t'_{mp})
\end{aligned}
\tag{38}
$$

These tensor operations are then converted into *einsum* functions. The problem is solved for by minimizing the energy with respect to the amplitudes

$$
\frac{\partial E}{\partial t_{ij}} = \frac{\partial E}{\partial t_{ijkl}} = \frac{\partial E}{\partial t'_{ij}} = \frac{\partial E}{\partial t'_{ijkl}} = 0 \tag{39}
$$

The total particle number must be then constrained at the same time

$$
\langle \hat{N} \rangle = \lambda_i \langle -|e^{\hat{T}'} e^{-\hat{T}} \hat{d}_i^\dagger \hat{d}_i e^{\hat{T}}|-\rangle = \lambda_i (-t_{ij} t'_{ij} + \frac{1}{6} t_{ijkl} t'_{ijkl}) \tag{40}
$$

Here the vector λ_i represents the fact that in the particle-hole formalism, the number operator is a bit different

$$\hat{N} = \sum_{\mathbf{k}} \hat{d}^\dagger_{\mathbf{k},+} \hat{d}_{\mathbf{k},+} - \sum_{\mathbf{k}} \hat{d}^\dagger_{\mathbf{k},-} \hat{d}_{\mathbf{k},-} = \lambda_i \hat{d}^\dagger_i \hat{d}_i \tag{41}$$

Just as before, the number operator expression can be converted to *einsum* operations

```
result -= einsum('i,ij,ij', L, T1, X1)
result += einsum('i,ijkl,ijkl', L, T2, X2) / 6.0
```

Thus a unconstrained minimization problem of the grand canonical Hamiltonian [28] can be formulated, to be numerically solved in the next subsection

$$\delta\langle -|\hat{H} \overbrace{-\gamma(\hat{N} - N)}^{\text{Chemical potential}}|-\rangle = 0 \tag{42}$$

Here γ is an arbitrary simulation parameter and $\mu = -\gamma(\langle\hat{N}\rangle - N)$ is the chemical potential, also known as the Fermi level, and describes the energy up to which the system is filled with electrons. The filling N is varied in terms of a fraction of the total amount of sampled points N_0.

An interesting note is that extended coupled cluster singles are identical to the Hartree-Fock method and thus correlation effects can be studied with minimal extra effort. This is also one of the benefits for using ECCSD rather than normal coupled cluster, since coupled cluster singles take into account less transitions in comparison with Hartree-Fock. From the number operator expectation value expression above it can be also seen that coupled cluster restricts the system to a null particle number in the particle-hole formalism and thus doesn't allow symmetry-breaking, which is required to study phase transitions. While it is possible to implement coupled cluster on top of Hartree-Fock [12], this only provides a quantitative analysis.

Finally, to describe addition or removal of a particle with momentum **k**, instead of deriving the EOM framework for ECCSD, an approximate eigenvalue approach can be formed, similar to EOM singles, of momentum conserving states

$$\frac{O_{\mathbf{k},n_1,n_2}}{N_0} = \langle -|\hat{d}_{\mathbf{k},n_1} e^{\hat{T}'} e^{-\hat{T}} \hat{H} e^{\hat{T}} \hat{d}^\dagger_{\mathbf{k},n_2}|-\rangle \tag{43}$$

Thus another expression is required

$$\begin{aligned}\langle -|\hat{d}_a e^{\hat{T}'} e^{-\hat{T}} \hat{H} e^{\hat{T}} \hat{d}^\dagger_b|-\rangle = \epsilon_{ab} + \delta_{ab}(E + V_{aibi}) - 2V_{aibm} t_{km} t'_{ik} - V_{ijbm} t_{am} t'_{ij} + \\ + \frac{1}{2} V_{ijbo} t_{aklo} (2t'_{il} t'_{jk} + t'_{ijkl}) + \frac{1}{3} V_{aibo} t_{klmo} t'_{iklm}\end{aligned} \tag{44}$$

In comparison with EOM, it is assumed that the amplitudes don't change with the addition of another particle, which is a reasonable approximation, since one particle is added, as will be seen in the next sections, to a few hundred.

3.3 Numerical Simulations with PyTorch

As previously mentioned, the problem above is solved via unconstrained minimization. Usually a root solver, as was seen in the previous section, Monte Carlo sampling [43], [44] or even quantum computing [45] can be utilized to numerically solve for the amplitudes. The PyTorch package [46] is used for machine learning purposes, a significant part of it being numeric manipulation of large scale tensors and minimization. One of the functionalities present in it is automatic differentiation [14], which uses computational graphs to symbolically evaluate derivatives at runtime. Thus it is used here in tandem with one of the built-in optimization routines to perform ECCSD simulations with minimal extra effort.

To gain more stability in the numerics, the optimization condition is changed to have a more pronounced minima and avoid falls to infinity

$$\langle -|\hat{H} - \gamma(\hat{N} - N)|-\rangle \;\rightarrow\; \langle \hat{H}\rangle + \gamma(\langle \hat{N}\rangle - N)^2 \tag{45}$$

On the numerical side of things, it is interesting to note that the order of which tensors are supplied, as well as a few other optional arguments, can greatly reduce the computation time of an *einsum* function. Thus all of them were funneled through the opt-einsum package [47] for automatic optimization. This package uses several path finding algorithms to optimize the contraction order for expression's supplied to the *einsum* function.

The stochastic gradient descent method, available in PyTorch, was used for these simulations with step sizes of $10^{-2} \sim 10^{-4}$. While not explored here, it might be possible to gain acceleration by implementing a line search algorithm [48] for dynamic and more appropriate step size estimates. The initial anti-symmetric tensors were filled with a small constant of 10^{-1} for singles and 10^{-4} for doubles, corresponding to the mean values of these tensors from trial simulations. This resulted in simulations requiring $\sim 10^1$ steps. In the case of single layer graphene, a value of unity for γ was satisfactory to reach the optimal characteristics above and it was verified that the chemical potential μ was invariant with respect to changes in γ.

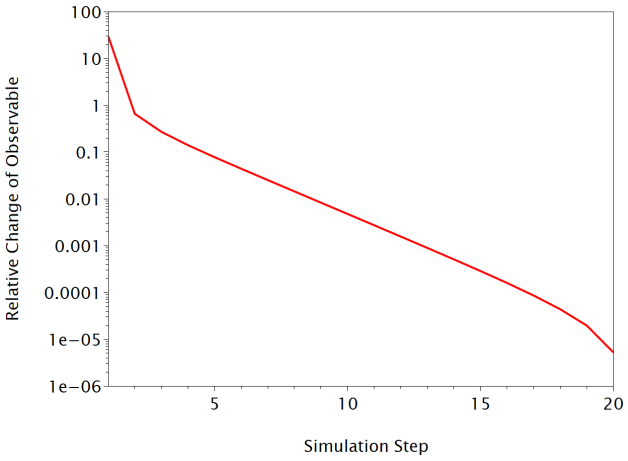

Fig. 10. An example dynamic of the ECCSD simulation convergence. This behaviour was observed for the particle number and ground state energy.

When supplying ECCSD equations with amplitudes, it is important to retain the anti-symmetry. This was done by converting the amplitude tensors at the beginning of each step via

$$T^A_{i_1,\ldots,i_p} = \frac{1}{p!}\sum_\alpha \text{sgn}(\alpha)\, T_{i_{\alpha(1)},\ldots i_{\alpha(p)}}. \tag{46}$$

Here α denotes all permutations of indices i_p and the respective sign change is encompassed in $\text{sgn}(\alpha)$ for every paired swapped. In the case of a matrix this would produce $T^A_{ij} = \frac{T_{ij}-T_{ji}}{2}$.

The convergence of an observable, such as the energy or particle number, is characterised by an initial bump, followed by a constant logarithmic convergence, during which the relative difference of reaches the threshold of 10^{-6} between steps and is terminated. An example of this dynamic is shown in Fig. 10. Note that the precision of the 32 bit floating point numbers, used in these simulations, is around 7 digits.

Moving on to single layer graphene, ECCS energy convergence with respect to the point sampling characteristic N_k is shown in Fig. 11 for fillings $N = \pm 1.0 N_0$. This is done separately for the interacting and non-interacting cases.

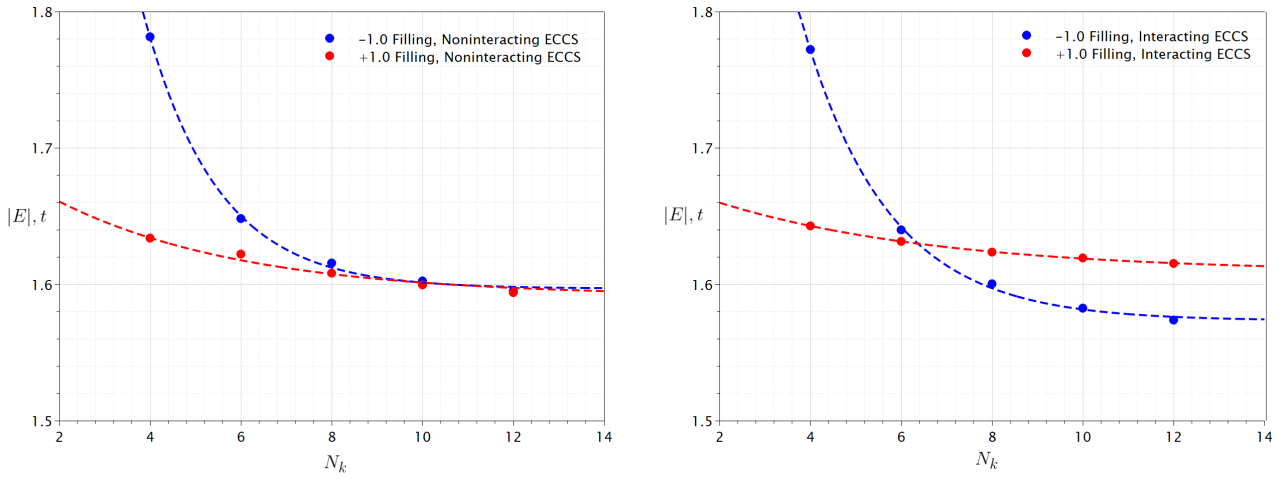

Fig. 11. ECCS energy convergence with respect to the point sampling characteristic N_k for fillings $N = \pm 1.0 N_0$. Interacting and non-interacting cases are shown separately.

In order to extract higher precision values, extrapolation was performed using curves of the form $y = A + \frac{B}{C^{D+x}}$ and gave relative errors of approximately $2 \cdot 10^{-3}$ for asymptotic values. If a qualitative picture is defined at 10% deviation from the asymptotic value, non-interacting ECCS can be said to give this at $N_k = 4$ and interacting ECCS at $N_k = 12$. This corresponds to 24 and 264 sampling points per band across the first Brillouin zone, respectively.

The positive filling is seen to have much faster convergence, in comparison with the negative one. This is easily understood from the fact that a $N = +1.0 N_0$ filling is closer to an empty system than $N = -1.0 N_0$. Both of the fillings are calculated to have the same potential shift of $|\Delta E| = 0.024t$

from the non-interacting ECCS energy $E = 1.597t$, but with an opposite sign. This contribution is calculated to account for 1.5% of the total energy and translates into the band gap as well, displayed in Fig. 12.

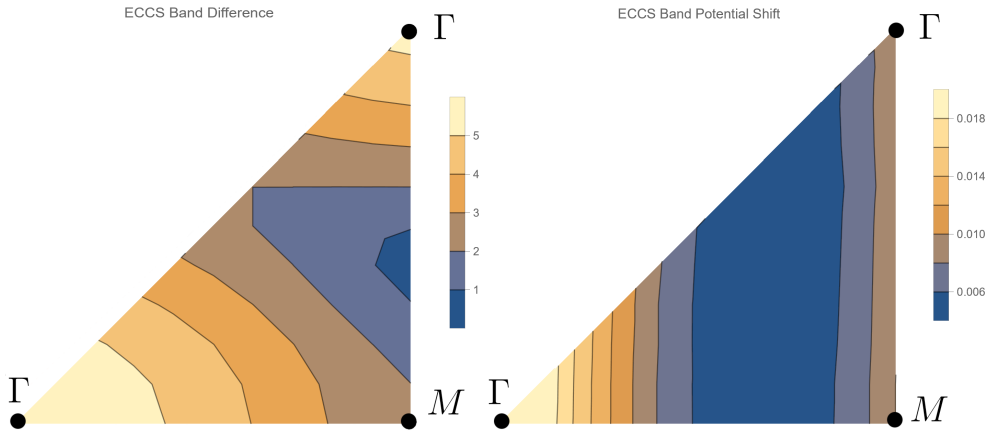

Fig. 12. ECCS band gap in the symmetric quarter of the first Brillouin zone. The magnitude of the potential shift for $N = \pm 1.0 N_0$ fillings is shown separately. A total of 66 points per band were sampled across the first Brillouin zone.

Addition of the electrostatic potential causes the bands to have a shift of around 1% on average, more pronounced at the Γ symmetry points, where the electrostatic potential is most significant. The bands at the Dirac point overlap at a positive filling and move away from each other in the case of a negative one, with the existence of this effect having been shown [49] experimentally. The chemical potential at $N = \pm 1.0 N_0$ fillings was calculated to be $\mu_- = -0.0108t$ and $\mu_+ = 0.0122t$, signifying the breaking of particle-hole symmetry. This leads to a Dirac band gap and chemical potential ratio of approximately 2.

Further, the convergence of the ECCSD energy is displayed in Fig. 13 for filling $N = +1.0 N_0$. As discussed above, the of case $N = -1.0 N_0$ produces anti-symmetric results. A qualitative picture is estimated to be given at $N_k = 19$ and an order of magnitude one at $N_k = 10$, which respectively corresponds to 684 and 180 sampling points per band across the first Brillouin zone, of which a third is actually sampled in these simulations.

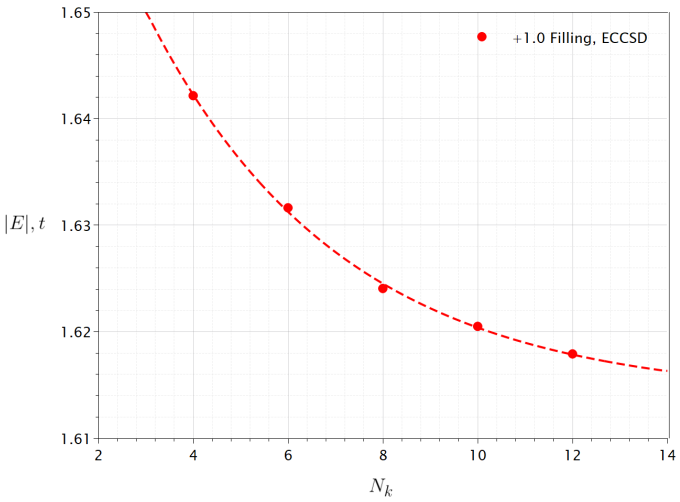

Fig. 13. ECCSD energy convergence with respect to point sampling characteristic N_k for filling $N = +1.0N_0$.

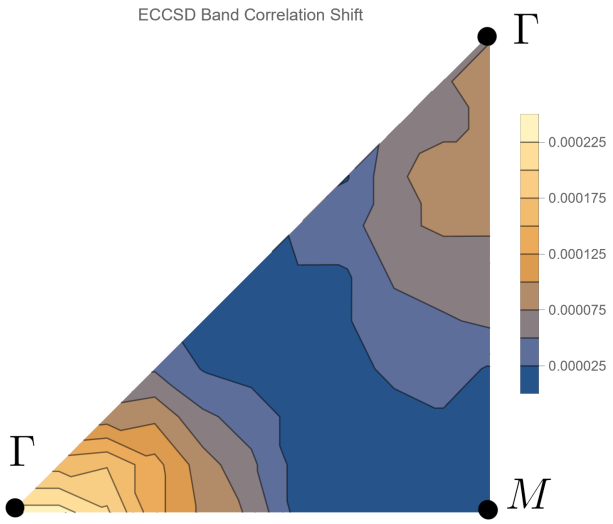

Fig. 14. Correlation shift of the ECCSD band gap in the symmetric quarter of the first Brillouin zone. This is in the case of filling $N = +1.0N_0$.

Combining ECCS values, the correlation energy shift is calculated to be $\Delta E = 0.006t$, which accounts for approximately 20% of the potential energy. It can be observed to carry over to the band gap correlation shift, displayed in Fig. 14. The band gap correlation effects are an order of magnitude smaller than of the ground state energy, most likely caused by the fact that an individual particle is described, in comparison to a entire collection of particles. Hence this ratio is of the same order of magnitude as the number of particles. Correlations are seen to be most significant where the potential is the largest - the Γ symmetry point, which is a trivial conclusion. Nevertheless, it is interesting that the Dirac point contains some correlation effects as well, about twice as small. The chemical potential is calculated to be $\mu_+ = 0.0186t$, which, in comparison to its ECCS value, corresponds to an increase of approximately 30% signifying an increased filling of the conduction band due to correlation effects.

4 Study of Correlation Effects in Twisted Bilayer Graphene

The previously developed ECCSD method is applied to twisted bilayer graphene. A low energy, continuum model is used for describing this system at small twist angles. Energies, chemical potentials and band structures at the magic angle are reported for a filling that is known to manifest the insulating-to-superconducting phase transition.

4.1 The Bistritzer-MacDonald Model

Twisted bilayer graphene (TBG) is created by twisting two graphene sheets with respect to each other. This creates a supercell with $\sim 10^4$ atoms for the first magic angle at $\theta \approx 1.1°$, where unconventional superconducting [18] and insulating [17] phases have been observed. In reciprocal space, this represents a very small Brillouin zone, as can be seen in Fig. 15. The corresponding reciprocal lattice vectors are then defined as $\mathbf{g_1} = \frac{4\pi}{a} \sin\left(\frac{\theta}{2}\right) \left(\frac{1}{\sqrt{3}}, 1\right)$ and $\mathbf{g_2} = \frac{8\pi}{a} \sin\left(\frac{\theta}{2}\right) \left(-\frac{1}{\sqrt{3}}, 0\right)$.

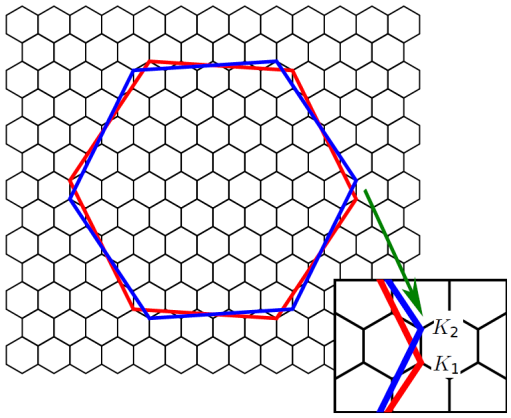

Fig. 15. The resulting Brillouin zone of twisted bilayer graphene at the first magic angle, caused by a small angle rotation of two graphene layers. Reprinted from Cea et al. [19].

One of the most widely used ways to model this material is the Bistritzer-MacDonald (BM) model [16]. It is a low energy continuum description of TBG, characterizing two isolated graphene sheets and a hopping process to the three equidistant Dirac points between the layers. Being suitable for the first magic angle, it is defined by a block Hamiltonian

$$\hat{H} = \begin{pmatrix} H_1 & U \\ U^\dagger & H_2 \end{pmatrix}_{ij} \hat{d}_i^\dagger \hat{d}_j \tag{47}$$

Here H_1 and H_2 represent the top and bottom layers, which are centered around their individual Dirac points, displayed in Fig. 15. For the first layer the momenta are sampled across the first Brillouin zone, as well as its copies in the first star of reciprocal lattice vectors $\{\pm\mathbf{g}_1, \pm\mathbf{g}_2, \pm\mathbf{g}_1 \pm \mathbf{g}_2\}$, which give the largest contribution [50]. Interactions with the second layer are described by U via the three closest harmonics. These couple the sites from the first layer to their neighboring ones in the second layer at $\{\mathbf{0}, -\mathbf{g}_1, -\mathbf{g}_1 - \mathbf{g}_2\}$, which are known to contribute the most [51]. The three harmonics are defined by

$$
\begin{aligned}
U(\mathbf{0}) &= \begin{pmatrix} a_1 & a_2 \\ a_2 & a_1 \end{pmatrix} \\
U(-\mathbf{g}_1) &= \begin{pmatrix} a_1 & a_2 e^{-2i\pi/3} \\ a_2 e^{2i\pi/3} & a_1 \end{pmatrix} \\
U(-\mathbf{g}_1 - \mathbf{g}_2) &= \begin{pmatrix} a_1 & a_2 e^{2i\pi/3} \\ a_2 e^{-2i\pi/3} & a_1 \end{pmatrix}
\end{aligned} \tag{48}
$$

In the BM model an isolated sheet of graphene is described by a Dirac-Hamiltonian expanded around the Dirac point $\mathbf{K}(\phi) = \frac{4\pi}{3a}(0, \sin(\phi))$. Due to the particle-hole formalism, used in ECCSD, it has to be diagonalized, as in the previous section, to expose the negative and positive energy bands

$$
\begin{pmatrix} 0 & q_x - iq_y \\ q_x + iq_y & 0 \end{pmatrix}\Bigg|_{\mathbf{q}=\mathbf{k}-\mathbf{K}(\phi)} \quad \rightarrow \quad \begin{pmatrix} -|\mathbf{k} - \mathbf{K}(\phi)| & 0 \\ 0 & |\mathbf{k} - \mathbf{K}(\phi)| \end{pmatrix} \tag{49}
$$

The elements of the new coupling matrices $U'_{ij} = \langle \psi_i | U | \psi_j \rangle$ are evaluated using the diagonalized basis functions

$$
|\psi_{\mathbf{q}=\mathbf{k}-\mathbf{K}(\phi)}\rangle_{\pm} = \frac{1}{\sqrt{2}} \begin{pmatrix} \pm\frac{q_x - iq_y}{\sqrt{q_x^2 + q_y^2}} \\ 1 \end{pmatrix} \tag{50}
$$

As per convention, the top layer is rotated by $\phi = -\frac{\theta}{2}$ and the bottom one by $\phi = \frac{\theta}{2}$. Electrostatic interactions can be added, as in the previous section, using Ewald summation, but this approach is quite computationally expensive and impractical. The latter is because most experiments [52] are conducted using a metallic gate, where TBG is enclosed between two layers of hexagonal boron nitride. Thus, in order to save computation time and make the simulation results more comparable with experiment, the double metallic gate potential [20] is used instead

$$
V(\mathbf{k}) \propto \frac{2\pi}{|\mathbf{a_1} \times \mathbf{a_2}|} \frac{\tanh(D|\mathbf{k}|)}{|\mathbf{k}|} \tag{51}
$$

Here the proportionality constant is calculated to be $0.21t$, the gate spacing $D = 160a$ and the TBG reciprocal unit cell area is given by $|\mathbf{a_1} \times \mathbf{a_2}| = \frac{\sqrt{3}a^2}{8\sin(\theta/2)^2}$. Finally, the Hubbard term is calculated to be $U = 0.0062t$.

The band structure is calculated as in the previous section, but now an eigenvalue problem is formed across all layers, harmonics and reciprocal lattice vector copies, resulting in a 56×56 matrix.

4.2 Numerical Results

From previous Hartree-Fock studies [20] it is known that the filling of interest is $N = +2.0N_0$, where the insulator phase transitions to a superconducting one. The above simulation setup might seem very costly, with 56 sites per momentum point. Fortunately, the first Brillouin zone is now approximately 80 times smaller in comparison with single layer graphene and, as a rough estimate, would require just a few sampling points for an equivalent precision analysis, when comparing with the last section.

Full first Brillouin zone 12-fold symmetry, implemented with $\mathbf{b_1} = \frac{\mathbf{g}'_1+\mathbf{g}'_2}{2}$, $\mathbf{b_2} = \frac{\mathbf{g}'_1-\mathbf{g}'_2}{6}$, is used in further calculations. Here $\mathbf{g}'_1 = \frac{4\pi}{a}\sin\left(\frac{\theta}{2}\right)(\frac{1}{\sqrt{3}}, 1)$ and $\mathbf{g}'_1 = \frac{4\pi}{a}\sin\left(\frac{\theta}{2}\right)(\frac{1}{\sqrt{3}}, -1)$ are rotated reciprocal lattice vectors. A first magic angle value of $\theta = 1.08^\circ$ has been previously reported for these parameters, in the case of Hartree-Fock, and thus is used in all further calculations. Note that, in the case of TBG, the simulation parameter γ had to be adjusted to values of $\sim 10^0$ for simulations to reach the accuracy and efficiency as in the previous section for single layer graphene.

In Fig. 16 the convergence of non-interacting and interacting ECCS energies are displayed for filling $N = +2.0N_0$ with respect to the total amount of sampled points.

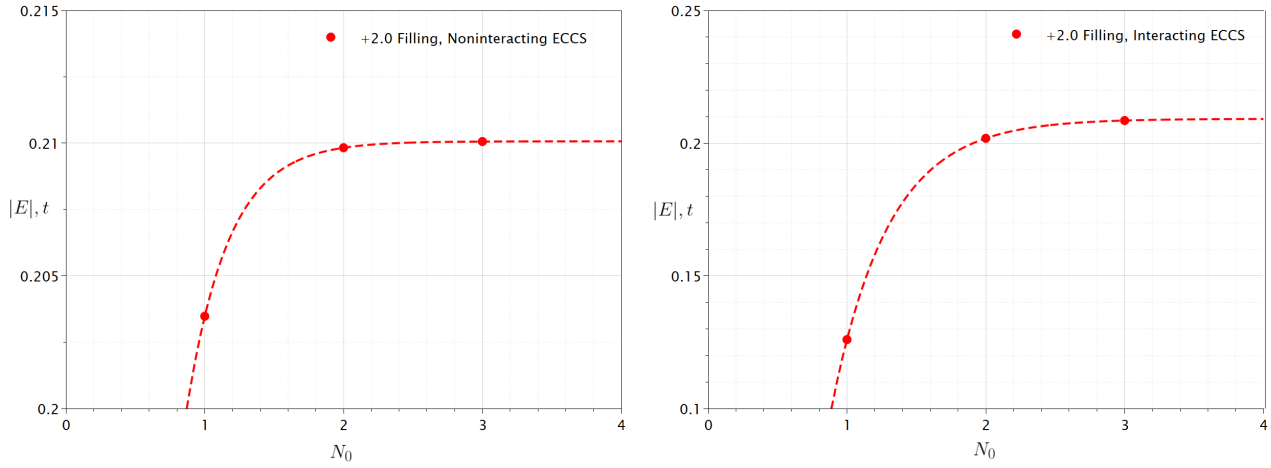

Fig. 16. ECCS energy convergence with respect to the amount of sampled point for filling $N = +2.0N_0$. The data is shown separately for the interacting and non-interacting cases.

As predicted previously, it was found that a few sampled points already resulted in convergence. After extrapolation this corresponded to a non-interacting ECCS energy of $E = 0.2101t$ with a positive potential shift of $\Delta E = 0.0009t$ equivalent to a contribution of 0.4%. This result is in accordance with a dimensional analysis estimate of $\frac{Ne^2}{\epsilon N_0\sqrt{|\mathbf{a_1}\times\mathbf{a_2}|}} \sim 20$ meV. Further calculations suggest that a qualitative picture is given at a single sampled point for non-interacting ECCS and 3 sampled points for ECCS, without extrapolation. The chemical potential is calculated to be $\mu = 0.0174t$.

Further, ECCSD energy convergence for the same filling of $N = +2.0N_0$ is displayed in Fig. 17 with respect to the total amount of sampled points. The correlation energy shift was calculated to be $\Delta E = 0.0006t$, representing a contribution of approximately 40% to the electrostatic energy. It was estimated that a qualitative picture is given at a total of four sampled points. An additional calculation of the chemical potential gives $\mu = 0.0209t$, which, in comparison with the value at ECCS truncation, shows an increase of approximately 20%.

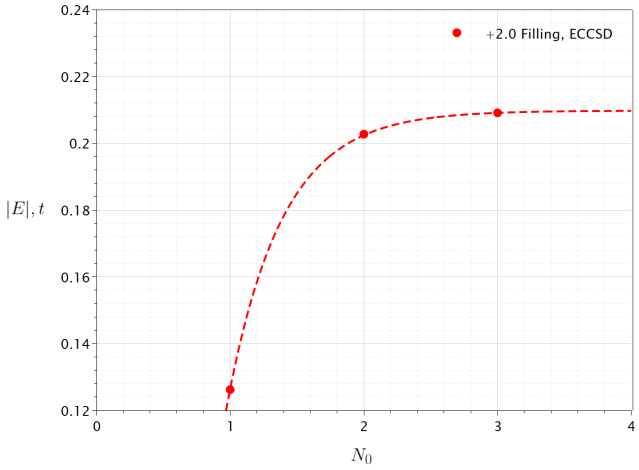

Fig. 17. ECCSD energy convergence with respect to the number of sampled points N_0 for filling $N = +2.0N_0$.

The three sampled points in the 12-fold Brillouin zone for this simulation are shown in Fig. 19 and the corresponding band structure is displayed in Fig. 18 with ground state energy acting as the baseline.

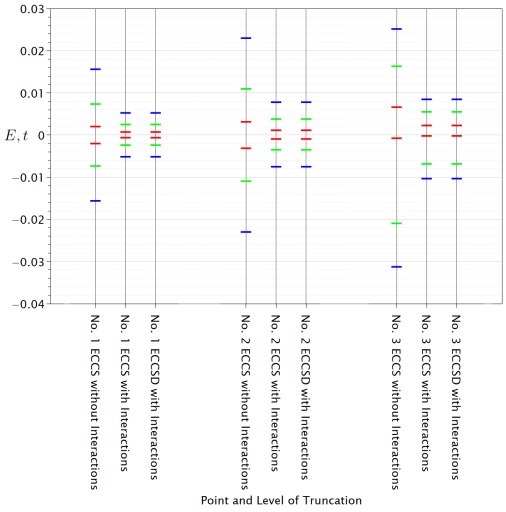

Fig. 18. The band structure of TBG at the three sampled points. Three levels of ECC truncation are shown.

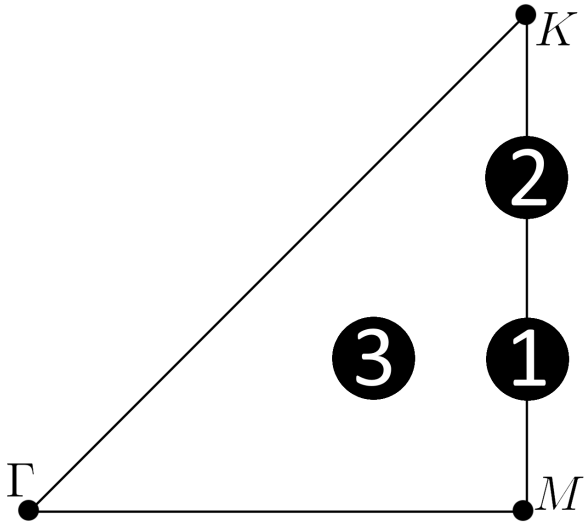

Fig. 19. Location of the three sampled points in the 12-fold symmetric triangle of the first Brillouin zone.

It is immediately visible that electrostatic effects are the leading cause of the insulating-to-superconducting phase transition in TBG, causing the bands to narrow around 3 times their nominal value. This is in accordance with previous Hartree-Fock studies. Further analysis shows that particle-hole symmetry is broken, which was only present along the $\Gamma - K - M$ symmetry line. Correlation effects are seen to shift the bands closer together by $\sim 10^{-3}$ of their magnitudes, thus having almost no influence. The cause of this is expected to be the same as discussed in the previous section for monolayer graphene. In tandem with the analysis of the chemical potential, it can be deduced that correlation effects increase the filling of the valence band relatively significantly. Thus the phase transition is expected to come at lower fillings, in a further development from other Hartree-Fock studies.

5 Conclusion and Further Work

In this dissertation, a short introduction to a few of the most widely known many-body techniques is presented - Hartree-Fock, coupled cluster and exact diagonalization. Further analysis is given of the correlation effects in a simple system - confined electrons in a one-dimensional box - for both ground and excited states. It is concluded that, while coupled cluster at doubles truncation provides a qualitative picture, it breaks down in describing regimes with strong correlation and excited states of large quantum numbers. Higher levels of truncation are suggested to remedy this.

Further, ECCSD theory is suggested to be a serious contender for studying phase transitions in strongly correlated systems, due to allowing symmetry-breaking in comparison with normal coupled cluster, which is only a small subset of ECC. A possible implementation of coupled cluster on top of Hartree-Fock is acknowledged, but is known to only provide a quantitative analysis. Therefore, a workflow for conducting simulations with ECCSD theory is developed, containing expressions for calculating the ground state energy, chemical potential and single particle excitation energies. This was accomplished by making use of the particle-hole formalism with half-filling serving as the vacuum, in order to produce manageable algebra. At singles truncation, the theory is discussed to be equivalent to Hartree-Fock. Additionally, automatic differentiation is shown to work well as an approach for conducting these simulations, meanwhile being suitable for any other theories as well.

An example application to single layer graphene is given, utilizing Ewald summation to account for the periodicity present in the system. This yielded a successful description of the cause of the electric field effect in the band structure at singles truncation. At doubles truncation correlation effects were shown to be of very minor impact to the band structure, but relatively significant in the calculation of the Fermi level.

A novel study of correlation effects in twisted bilayer graphene is presented as well. This was done using the BM model in a diagonalized basis with an added double metallic gate potential to account for electrostatic interactions in an experimental setting - sandwiched between hBN layers. Simulations at singles truncation agreed with previous Hartree-Fock studies in that electrostatic effects are the leading contribution of the insulating-to-superconducting phase transition, because of the significant narrowing of the gaps in the band structure. Correlation effects at doubles truncation showed insignificant contributions to the band structure, but a relatively significant increase of the Fermi level, indicating lower filling requirements for the phase transition.

The main bottleneck of the presented ECCSD workflow is the memory usage, because of its $O(N^4)$ scaling. Significant improvement on the computational cost of the ECCSD method can be achieved by implementing the following decomposition of the 4-rank doubles tensors

$$t_{ijkl} \to \tilde{t}^p_{ij} s^p \tilde{t}^p_{kl} \tag{52}$$

Here the dimensions of the vector s is the same as the amount of sites. This approximation is indirectly equivalent to momentum conservation and can be also done for the rank-4 potential tensor. For the coupled cluster doubles method, compression rates up to a few hundred are reported [53]. More recent work [54] has developed the tensor hypercontraction method, which decomposes the above rank-3 tensors even further to matrices using standard numerical algorithms.

With more computational resources and efficient software available, spin and valley effects can be described and their correlation effects studied, causing the amount of sites to enlarge fourfold. The former can be done within the BM model by the Hubbard term being present only for the same site interaction, but with opposite spin

$$\hat{H}_{\text{spin}} = U\hat{n}_{i,\downarrow}\hat{n}_{i,\uparrow} \tag{53}$$

This effect has been shown to create electronically tunable antiferromagnetic and ferromagnetic phases [55] that can be used to study spin-liquids, with doping potentially giving rise to high temperature superconductivity.

The latter, valley symmetry, is built into the BM model and consideration of valley polarization effects requires a slightly modified [22] continuum model. This can be done by introducing valley $\xi = \{\pm 1\}$ parameterization in the description of a single sheet of graphene

$$\begin{pmatrix} -|\mathbf{k} - \mathbf{K}(\phi)| & 0 \\ 0 & |\mathbf{k} - \mathbf{K}(\phi)| \end{pmatrix} \quad \rightarrow \quad \xi \begin{pmatrix} -|\mathbf{k} - \xi\mathbf{K}(\phi)| & 0 \\ 0 & |\mathbf{k} - \xi\mathbf{K}(\phi)| \end{pmatrix} \tag{54}$$

Additionally, off-diagonal and distance dependent hopping terms have to be introduced as well, at the real space stage of the model

$$\hat{H}_{\text{valley}} = t(\mathbf{r}_i - \mathbf{r}_j)\hat{d}_j^{\dagger}\hat{d}_i \tag{55}$$

Here $t(\mathbf{r})$ can be calculated, for example, from Slater-Koster rules. Consideration of valley polarization is known to give rise to secondary effects and [56] to the Josephson diode effect, but doesn't exhibit as much interesting phenomena as the addition of spin effects or TBG itself. Thus it can and is often neglected.

In a final note, it should be obvious that the ECCSD technique, described in this dissertation, can be applied to study phase transitions of any correlated materials [57], for example, "heavy fermion" materials, iron pnictide high temperature superconductors, layered dichalcogenides, the correlated oxides VO_2 and Fe_3O_4 as well as many others.

References

[1] D. R. Hartree, “The wave mechanics of an atom with a non-coulomb central field. part i. theory and methods,” *Mathematical Proceedings of the Cambridge Philosophical Society*, vol. 24, pp. 89–110, 1928 (cited on p. 6).

[2] P. Hohenberg and W. Kohn, “Inhomogeneous electron gas,” *Phys. Rev.*, vol. 136, pp. 864–871, 1964 (cited on p. 6).

[3] J. Cizek, “On the correlation problem in atomic and molecular systems. calculation of wavefunction components in ursell-type expansion using quantum-field theoretical methods,” *Journal of Chemical Physics*, vol. 45, pp. 4256–4266, 1966 (cited on p. 6).

[4] M. D. Donsker and M. Kac, “A sampling method for determining the lowest eigenvalue and the principal eigenfunction of schroedinger’s equation,” *Journal of research of the National Bureau of Standards*, vol. 44, p. 551, 1950 (cited on p. 6).

[5] G. Carleo and M. Troyer, “Solving the quantum many-body problem with artificial neural networks,” *Science*, vol. 355, pp. 602–606, 2016 (cited on p. 6).

[6] J. Arponen, “Variational principles and linked-cluster exp s expansions for static and dynamic many-body problems,” *Annals of Physics*, vol. 151, pp. 311–382, 1983 (cited on pp. 6, 19).

[7] J. S. Arponen, R. F. Bishop, and E. Pajanne, “Extended coupled-cluster method. i. generalized coherent bosonization as a mapping of quantum theory into classical hamiltonian mechanics.,” *Physical review. A, General physics*, vol. 36 6, pp. 2519–2538, 1987 (cited on p. 6).

[8] ——, “Extended coupled-cluster method. ii. excited states and generalized random-phase approximation.,” *Physical review. A, General physics*, vol. 36 6, pp. 2539–2549, 1987 (cited on p. 6).

[9] Arponen, Bishop, Pajanne, and Robinson, “Extended coupled-cluster method. iii. zero-temperature hydrodynamics of a condensed bose fluid.,” *Physical review. A, General physics*, vol. 37 4, pp. 1065–1086, 1988 (cited on p. 6).

[10] Robinson, Bishop, and Arponen, “Extended coupled-cluster method. iv. an excitation energy functional and applications to the lipkin model.,” *Physical review. A, General physics*, vol. 40 8, pp. 4256–4276, 1989 (cited on p. 6).

[11] A. Laestadius and S. Kvaal, “Analysis of the extended coupled-cluster method in quantum chemistry,” *SIAM J. Numer. Anal.*, vol. 56, pp. 660–683, 2017 (cited on p. 6).

[12] A. Papastathopoulos-Katsaros, C. A. Jimenez-Hoyos, T. M. Henderson, and G. E. Scuseria, “Coupled cluster and perturbation theories based on a cluster mean-field reference applied to strongly correlated spin systems.,” *Journal of chemical theory and computation*, 2021 (cited on pp. 6, 22).

[13] A. Griewank and A. Walther, “Evaluating derivatives - principles and techniques of algorithmic differentiation, second edition,” in *Frontiers in applied mathematics*, 2000 (cited on p. 6).

[14] A. Paszke, S. Gross, S. Chintala, *et al.*, “Automatic differentiation in pytorch,” 2017 (cited on pp. 6, 23).

[15] J. M. B. L. dos Santos, N. M. R. Peres, and A. H. C. Neto, “Graphene bilayer with a twist: Electronic structure.,” *Physical review letters*, vol. 99 25, p. 256 802, 2007 (cited on p. 6).

[16] R. Bistritzer and A. H. Macdonald, “Moire bands in twisted double-layer graphene,” *Proceedings of the National Academy of Sciences*, vol. 108, pp. 12 233–12 237, 2010 (cited on pp. 6, 27).

[17] Y. Cao, V. Fatemi, A. Demir, *et al.*, “Correlated insulator behaviour at half-filling in magic-angle graphene superlattices,” *Nature*, vol. 556, pp. 80–84, 2018 (cited on pp. 6, 27).

[18] Y. Cao, V. Fatemi, S. Fang, *et al.*, “Unconventional superconductivity in magic-angle graphene superlattices,” *Nature*, vol. 556, pp. 43–50, 2018 (cited on pp. 6, 27).

[19] T. Cea, N. R. Walet, and F. Guinea, “Electronic band structure and pinning of fermi energy to van hove singularities in twisted bilayer graphene: A self-consistent approach,” *Physical Review B*, 2019 (cited on pp. 6, 27).

[20] T. Cea, P. A. Pantale’on, N. R. Walet, and F. Guinea, “Electrostatic interactions in twisted bilayer graphene,” *Nano Materials Science*, 2021 (cited on pp. 6, 28, 29).

[21] F. M. Faulstich, K. D. Stubbs, Q. Zhu, *et al.*, “Interacting models for twisted bilayer graphene: A quantum chemistry approach,” *Physical Review B*, 2022 (cited on p. 6).

[22] A. Jimeno-Pozo, Z. A. H. Goodwin, P. A. Pantaleón, *et al.*, “Short versus long range exchange interactions in twisted bilayer graphene,” *Advanced Physics Research*, 2023 (cited on pp. 6, 32).

[23] C. J. C. Scott and G. H. Booth, “Rigorous screened interactions for realistic correlated electron systems,” 2023 (cited on p. 6).

[24] R. Shankar, *Principles of Quantum Mechanics*. Plenum Press, New York, 1994 (cited on p. 7).

[25] D. S. Koltun and J. M. Eisenberg, *Quantum Mechanics of Many Degrees of Freedom*. John Wiley & Sons, Inc., 1988 (cited on p. 8).

[26] P. Virtanen, R. Gommers, T. E. Oliphant, *et al.*, "Scipy 1.0: Fundamental algorithms for scientific computing in python," *Nature Methods*, vol. 17, pp. 261–272, 2019 (cited on pp. 8, 9).

[27] A. Meurer, C. P. Smith, M. Paprocki, *et al.*, "Sympy: Symbolic computing in python," *PeerJ Prepr.*, vol. 4, e2083, 2017 (cited on p. 9).

[28] A. Fetter and J. Walecka, *Quantum Theory of Many-Particle Systems*. McGraw-Hill Book Co., New York, 1971 (cited on pp. 10, 22).

[29] I. Shavitt and R. J. Bartlett, *Many-Body Methods in Chemistry and Physics: MBPT and Coupled-Cluster Theory*. Cambridge University Press, 2009 (cited on p. 10).

[30] A. E. DePrince and N. C. Rubin, *Pdaggerq*, 2021. [Online]. Available: `https://github.com/edeprince3/pdaggerq` (cited on p. 11).

[31] C. R. Harris, K. J. Millman, S. van der Walt, *et al.*, "Array programming with numpy," *Nature*, vol. 585, pp. 357–362, 2020 (cited on p. 11).

[32] C. Yang, J. Brabec, L. Veis, D. B. Williams-Young, and K. Kowalski, "Solving coupled cluster equations by the newton krylov method," *Frontiers in Chemistry*, vol. 8, 2020 (cited on p. 11).

[33] J. F. Stanton and R. J. Bartlett, "The equation of motion coupled-cluster method. a systematic biorthogonal approach to molecular excitation energies, transition probabilities, and excited state properties," *Journal of Chemical Physics*, vol. 98, pp. 7029–7039, 1993 (cited on p. 11).

[34] F. Jensen, *Introduction to Computational Chemistry*. John Wiley & Sons Ltd, 2007 (cited on p. 12).

[35] P. P. Ewald, “Die berechnung optischer und elektrostatischer gitterpotentiale,” *Annalen der Physik*, vol. 369, pp. 253–287, (cited on p. 17).

[36] F. E. Harris, “Ewald summations in systems with two-dimensional periodicity,” *International Journal of Quantum Chemistry*, vol. 68, pp. 385–404, 1998 (cited on p. 17).

[37] T. O. Wehling, E. Şaşıoğlu, C. Friedrich, A. I. Lichtenstein, M. I. Katsnelson, and S. Blugel, “Strength of effective coulomb interactions in graphene and graphite.,” *Physical review letters*, vol. 106 23, p. 236 805, 2011 (cited on p. 17).

[38] A. Bakhshandeh and Y. Levin, “Widom insertion method in simulations with ewald summation.,” *The Journal of chemical physics*, vol. 156 13, p. 134 110, 2022 (cited on p. 18).

[39] A. H. C. Neto, F. Guinea, N. M. R. Peres, K. S. Novoselov, and A. K. Geim, “The electronic properties of graphene,” *Reviews of Modern Physics*, vol. 81, pp. 109–162, 2007 (cited on p. 18).

[40] H. J. Monkhorst and J. D. Pack, “Special points for brillouin-zone integrations,” *Physical Review B*, vol. 13, pp. 5188–5192, 1976 (cited on p. 19).

[41] J. D. Pack and H. J. Monkhorst, “”special points for brillouin-zone integrations” — a reply,” *Physical Review B*, vol. 16, pp. 1748–1749, 1977 (cited on p. 19).

[42] W. R. Inc., *Mathematica, Version 13.2*, Champaign, IL, 2022. [Online]. Available: `https://www.wolfram.com/mathematica` (cited on p. 20).

[43] G. H. Booth, A. J. W. Thom, and A. Alavi, “Fermion monte carlo without fixed nodes: A game of life, death, and annihilation in slater determinant space.,” *The Journal of chemical physics*, vol. 131 5, p. 054 106, 2009 (cited on p. 23).

[44] A. J. W. Thom, “Stochastic coupled cluster theory.,” *Physical review letters*, vol. 105 26, p. 263 004, 2010 (cited on p. 23).

[45] J. Romero, R. Babbush, J. R. McClean, C. Hempel, P. J. Love, and A. Aspuru-Guzik, “Strategies for quantum computing molecular energies using the unitary coupled cluster ansatz,” *Quantum Science and Technology*, vol. 4, 2017 (cited on p. 23).

[46] A. Paszke, S. Gross, F. Massa, *et al.*, “Pytorch: An imperative style, high-performance deep learning library,” in *Neural Information Processing Systems*, 2019 (cited on p. 23).

[47] D. G. A. Smith and J. Gray, “Opt_einsum - a python package for optimizing contraction order for einsum-like expressions,” *Journal of Open Source Software*, vol. 3, no. 26, p. 753, 2018 (cited on p. 23).

[48] O. Nelles, in *Optimization Techniques and Applications with Examples*. John Wiley & Sons, Ltd, 2018 (cited on p. 23).

[49] K. S. Novoselov, S. Duttasinha, S. V. Morozov, *et al.*, “Electric field effect in atomically thin carbon films,” *Science*, vol. 306, pp. 666–669, 2004 (cited on p. 25).

[50] F. Guinea and N. R. Walet, “Electrostatic effects, band distortions, and superconductivity in twisted graphene bilayers,” *Proceedings of the National Academy of Sciences of the United States of America*, vol. 115, pp. 13 174–13 179, 2018 (cited on p. 27).

[51] ——, “Continuum models for twisted bilayer graphene: Effect of lattice deformation and hopping parameters,” *Physical Review B*, 2019 (cited on p. 27).

[52] Z. A. H. Goodwin, V. Vitale, F. Corsetti, D. K. Efetov, A. A. Mostofi, and J. Lischner, “Critical role of device geometry for the phase diagram of twisted bilayer graphene,” *Physical Review B*, 2019 (cited on p. 28).

[53] T. Kinoshita, O. Hino, and R. J. Bartlett, “Singular value decomposition approach for the approximate coupled-cluster method,” *Journal of Chemical Physics*, vol. 119, pp. 7756–7762, 2003 (cited on p. 32).

[54] F. Hummel, T. Tsatsoulis, and A. Gruneis, “Low rank factorization of the coulomb integrals for periodic coupled cluster theory.,” *The Journal of chemical physics*, vol. 146 12, p. 124 105, 2016 (cited on p. 32).

[55] L. A. Gonzalez-Arraga, J. L. Lado, F. Guinea, F. Guinea, and S. J. Pablo, “Electrically controllable magnetism in twisted bilayer graphene.,” *Physical review letters*, vol. 119 10, p. 107 201, 2017 (cited on p. 32).

[56] J.-X. Hu, Z. Sun, Y. Xie, and K. T. Law, “Josephson diode effect induced by valley polarization in twisted bilayer graphene.,” *Physical review letters*, vol. 130 26, p. 266 003, 2022 (cited on p. 32).

[57] E. Morosan, D. Natelson, A. H. Nevidomskyy, and Q. Si, “Strongly correlated materials,” *Advanced Materials*, vol. 24, 2012 (cited on p. 32).